Chapter 6

Test of the CsI(Tℓ) Calorimeter Performance by Photon Beam.

6.1 Motivation

In the BELLE experiment, the electromagnetic calorimeter is responsible for the detection of photons and electrons in a wide energy range. The minimum energy is 20 MeV for photons from π^0 decay and the maximum energy is 8 GeV for electrons from Bhabha scattering. A good energy resolution, linearity and position resolution is required to detect such photons in a wide energy range.

We used a wide energy range photon beam of the VEPP-4M collider at Budker Institute of Nuclear Physics (BINP), Russia to measure the performance of 6 × 6 matrix of CsI(Tℓ) counters. The aims of the experiment are

- tests of the counters performance as well as final electronics,
- development of the calibration procedure, clustering and analysis method,
- investigation of the properties of the Monte Carlo simulation programs by comparing with real data.

6.2 Photon Beam

We used two sources of photon beam in this measurement. One is a backward scattered laser light by an ROKK-1M electron beam in VEPP-4M electron-positron storage ring in a Compton scattering process; $\gamma(2.33\text{ eV}) + e^- \to \gamma + e^-(\text{tagged})$ (Fig 6.1)(a). The

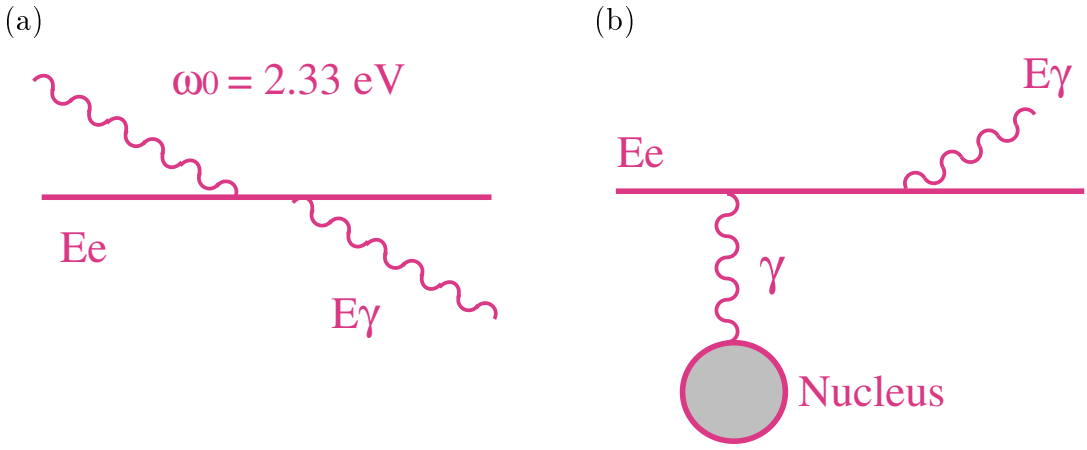

Figure 6.1: (a) Compton scattering and (b) Bremsstrahlung scattering.

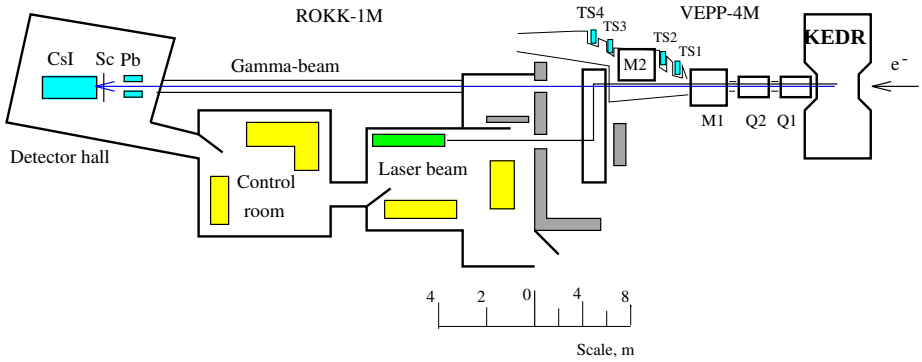

Figure 6.2: Layout of the photon beam line.

energy of the photon is calculated by measuring the energy of the scattered electron using the tagging system. The other source is the Bremsstrahlung photon generated by the collision of the electron beam and the residual gas nuclei in the vacuum chamber of the accelerator; $e^- + \text{Nucleus} \rightarrow \gamma + e^- + \text{Nucleus}$(Fig 6.1).

A schematics of the photon beam line at ROKK-1M is shown in Fig 6.2 [65]. Primary photons with an energy of 2.33 eV are generated by Nd:YAG pulse laser. The photon is guided to the interaction point of VEPP-4M by a set of mirrors and makes a head-on collision with the electron beam. By the backward Compton scattering with electron, the laser photon receives a significant part of the electron energy E_{beam} and boosted back in the direction of initial electron beam. The energy of the photon is calculated in each event by measuring of the electron energy in the tagging system

(TS) placed in the straight section of the storage ring.

The tagging system consists of TS_1 to TS_4, each of which is consists of six double layers of drift tubes. The deflection of electron by the machine component magnet, Q1 and Q2 quadruples and M1 and M2 dipoles, is used to analyze the momentum. The resolution of the tagging system is determined by the magnetic structure of the interaction region of accelerators, electron beam parameters such as the angular and energy spread and the transverse size at the interaction point, the space resolution of the drift tube. The energy spectrum of the Compton scattered photon $F(E)$ is approximated for $E_c \ll E_{beam}$ by;

$$F(E) = N((E - \frac{E_c}{2})^2 + \frac{E_c^2}{4}). \tag{6.1}$$

where N is the normalization factor and E is the photon beam energy. The Compton edge energy E_c is calculated from the primary photon energy ω_0 and the electron beam energy as follows;

$$E_c = 4\gamma^2\omega_0/(1 + \frac{4\gamma\omega_0}{m_e}). \tag{6.2}$$

where γ is the relativistic factor of incoming electron and m_e is the electron mass.

The Bremsstrahlung cross section is described by the following formula [66];

$$d\sigma = 4Z^2 r_e^2 \alpha \frac{d\nu}{\nu}((1+\varepsilon^2)(\frac{\phi_{1(\xi)}}{4} - \frac{1}{3}lnZ - f(Z)) - \frac{2}{3}\varepsilon(\frac{\phi_2(\xi)}{4} - \frac{1}{3}lnZ - f(Z))), \tag{6.3}$$

Z : atomic number of the material,
r_e : electron classical radius (e^2/mc^2),
α : 1/137,
ε : E/E_0,
E_0 : total energy of the incident electron,
E : total energy of the scattered electron,
$f(Z)$: Coulomb correction factor,
$\phi_1(\xi)$, $\phi_2(\xi)$: screening function,

ξ is the screening parameter and given by the formula,

$$\xi = \frac{100 m_e c^2 h\nu}{E_0 E Z^{1/3}}, \tag{6.4}$$

$h\nu$: energy of photon

In the case of complete screening ($\xi = 0$), the cross section becomes

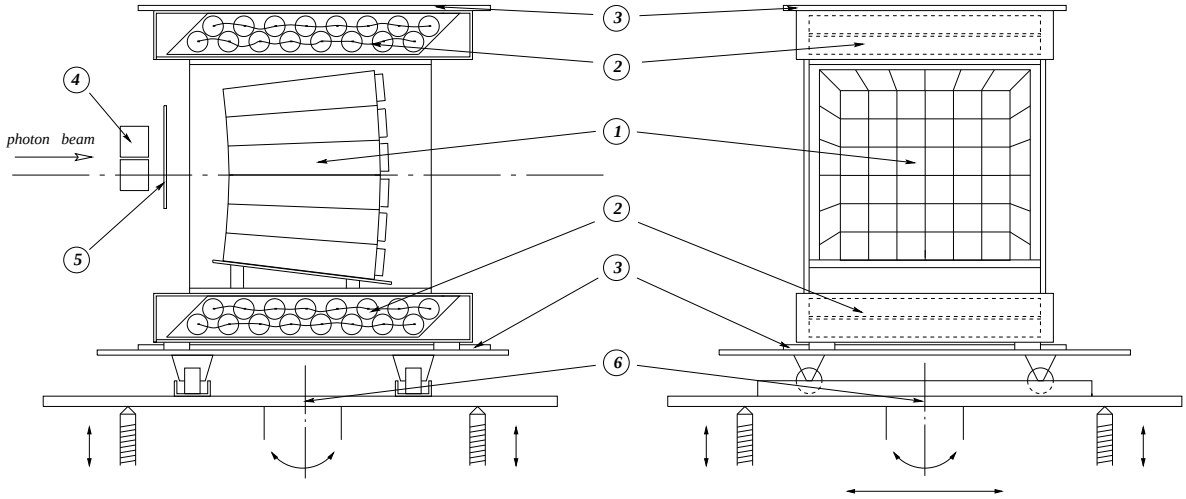

Figure 6.3: Experimental setup − 1. CsI(Tℓ) counters; 2. drift tube hodoscopes; 3. plastic scintillation counters for cosmic trigger; 4. lead collimator; 5. veto counter; 6. movable platform for the position adjustment.

$$d\sigma = 4Z^2 r_e^2 \alpha \frac{d\nu}{\nu}((1+\varepsilon^2 - \frac{2\varepsilon}{3})(ln(183Z{-}1/3) - f(Z)) + \frac{\varepsilon}{9}). \tag{6.5}$$

The spectrum is inversely proportional to the photon energy ν. The maximum energy of the photon in Bremsstrahlung is near to the incident electron energy. For the Bremsstrahlung photon, the edge value of the spectrum was used for the analysis but the tagging system was not used.

The rate of the Compton photon is proportional to the beam current, laser intensity and laser frequency. The laser was set at the maximum intensity and frequency (10kHz) and the timing is synchronized with a beam phase signal of $\sim$ 800 kHz. The electron beam current was limited at around 1 μA such that the number of interacted photons is kept less than 0.1 for each laser pulse. The transverse size of the photon beam is 2-4 cm at the CsI matrix and it is mainly determined by the electron beam parameters. The photon beam is injected to the front face of the CsI matrix.

6.3 Experimental Setup

The experimental setup is shown in Fig 6.3 and Fig. 6.4. The CsI(Tℓ) counters are piled in a 6 $\times$ 6 matrix and installed in a light shielded box. The box is placed on a

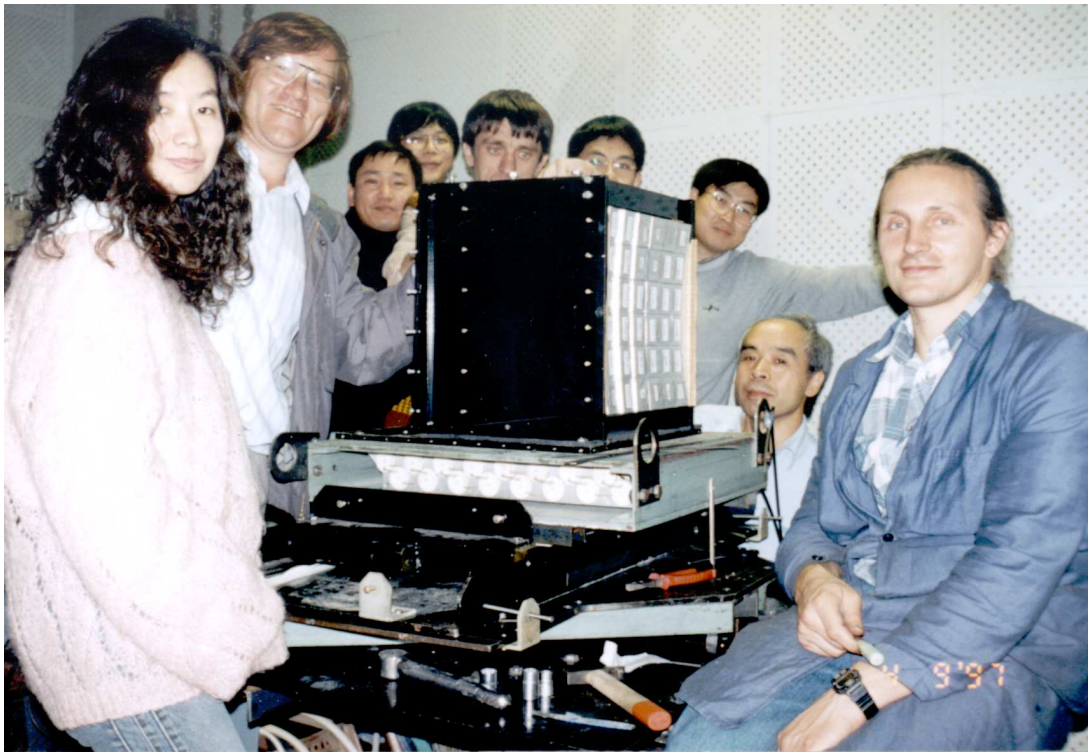

Figure 6.4: Beam test setup and crews.

movable table for the alignment to the photon beam. A plastic scintillation counter was installed in front of the matrix to veto photons converted in the output window of VEPP-4M and in the upstream air.

We used 36 crystals of the standard BELLE type produced at BINP. The dimension of the crystals is approximately 55 × 55 mm at the front end and 60 × 60 mm at the rear end. The length is 300 mm. The structure of the counter is described in Chapter 4. Aluminum sheets of 0.5 mm thickness are placed between the crystals to simulate the effect of compartment walls of the crystal container (see section 4.7).

For most of the data taking, the photon beam is injected to the center of the four central counters ((3,3)(3,4)(4,3)(4,4)). Then the signals from 3 × 3 or 5 × 5 counters are summed for the analysis. The heavily shaded area in Fig. 6.5 shows the region of 3 × 3 summation and the lightly shaded area is for 5 × 5 summation with the photon beam injected at the center of (4,4) crystal. All the counters are calibrated by the cosmic ray *in situ* and the central 16 counters are calibrated by the photon beam.

Two sets of drift tube hodoscopes are installed at the top and bottom of the matrix for the cosmic-ray calibration. Each set is composed of two layers of eight tubes, which are connected in sequence. The radius of the tube was 40 mm and the position along

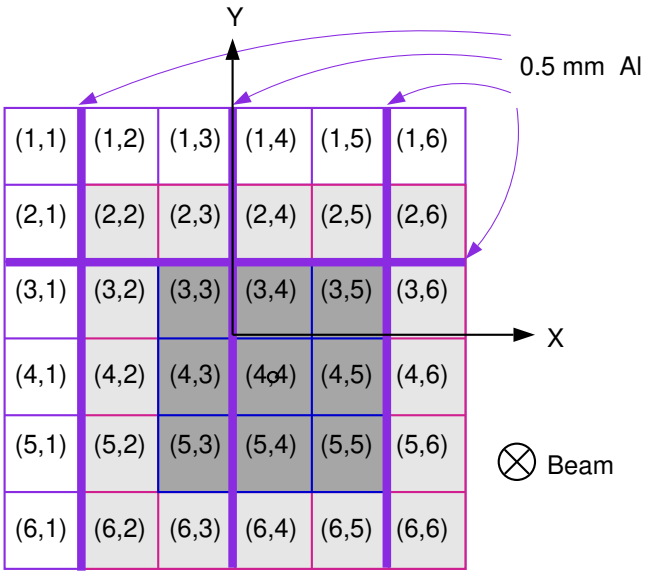

Figure 6.5: 6 × 6 CsI(Tℓ) matrix and crystal numbering (Front view).

the wire was determined with an accuracy of 15 mm by measuring the difference of the arriving time of the signal at the both ends of the wire. The plastic scintillation counters are used for triggering cosmic rays.

A schematics of the trigger and data acquisition system is shown in Fig. 6.6. For Compton runs, a trigger was produced by the coincidence of the scintillation counter signal placed behind of the TS drift tubes and the anti-signal from the veto counter And the signals from the CsI(Tℓ) matrix is used only for low energy. A beam crossing marker and a laser gate pulse are also required. The signal from the matrix is defined when an analog sum of the central 15 counters* produced by the STM module is above certain energy threshold. For Bremsstrahlung runs, the TS scintillator and the laser gate pulse were not required. A gate signal of 100 ns wide is generated by the trigger and is distributed to the shaper/QT module through the calibration module (CAL). The CAL module also generated the test pulse for the calibration of the electronics, LED driving pulse and supplied 60 V bias of the photodiode.

All the electronics used in the test beam are same as the production version except STM and CAL module. The two modules were CAMAC version prototype. The data acquisition from the FASTBUS TDC and the control of CAMAC modules are done by one-board SUN computer in VME system. The data taking rate was about 100 Hz for

*central 16 counters except (5,5).

the usual Compton runs. The temperature was continuously monitored also by SUN computer system.

6.4 Data Collection

Analysis	E_{beam}(MeV)	Compton Edge(MeV)
Energy calibration	4036.	508.3
Energy resolution and linearity	921.	29.4
	1206.	49.8
	1506.	76.8
	1810.	109.8
	3007.	291.5
	4036.	508.3
	5441.	884.7

Table 6.1: Summary of the beam setup in the beam test.

We took the data in September and October, 1997. All the data were collected at seven different settings of the electron beam energy. Both Compton photon and Bremsstrahlung photon data were obtained for each energy setting. Used electron beam energy and the corresponding Compton edge energy are listed in Table. 6.1. About 50k to 200k events were collected for each energy setting of Compton and Bremsstrahlung runs. The Compton photon of 508 MeV was used for the beam calibration. For this purpose, the beam was injected at the center of central 16 counters. The same photon energy was used for the measurement of the position dependence.

The pedestal and test pulse runs were done once every few hours during the beam time. The cosmic data were taken during the beam off time. The number of triggered events was 100k in average and it took 8 hours. The pedestal, test pulse and LED runs were also made regularly during the beam off time to check the electronics performance.

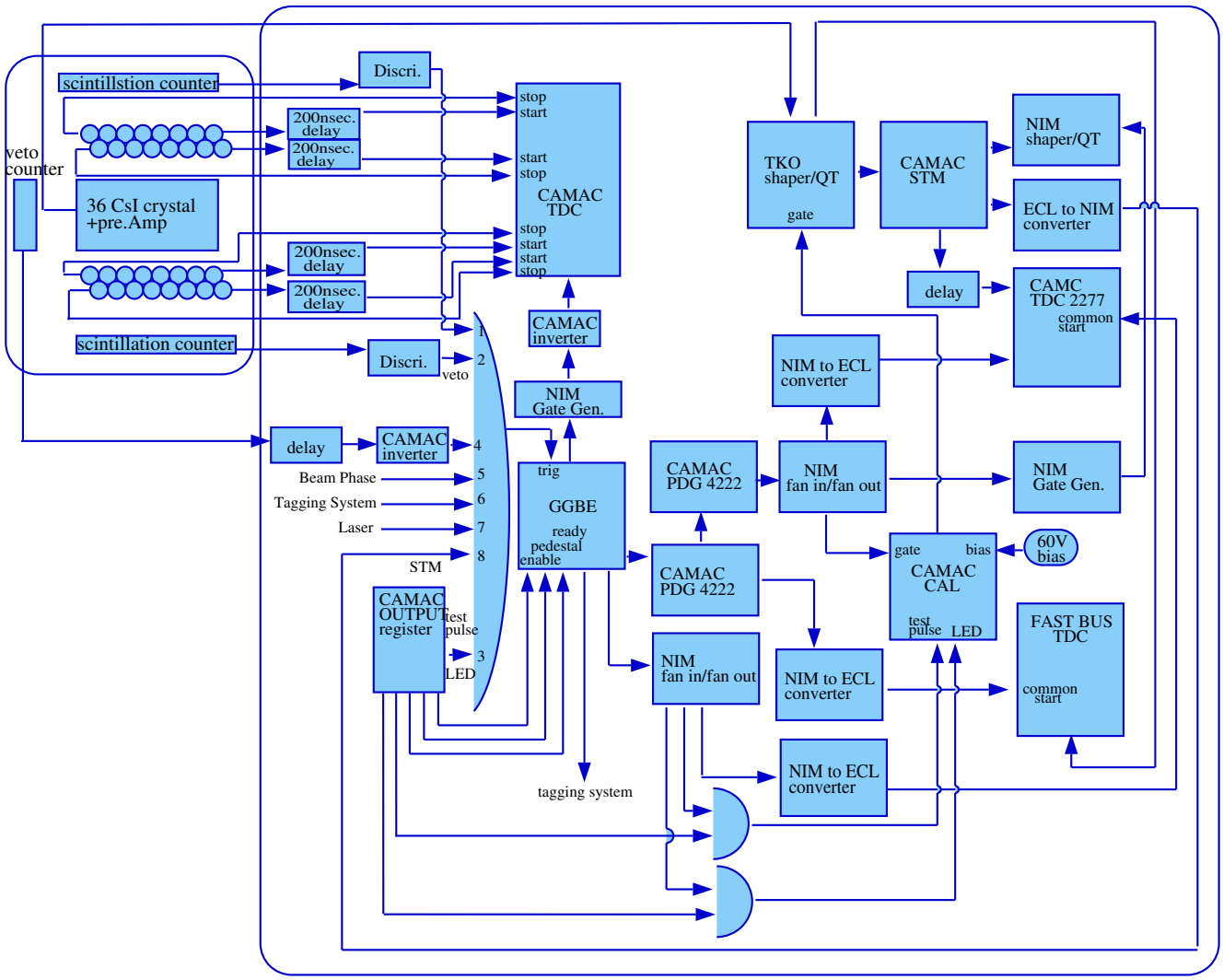

Figure 6.6: Schematics of trigger and data acquisition for the beam test.

(a) (b)

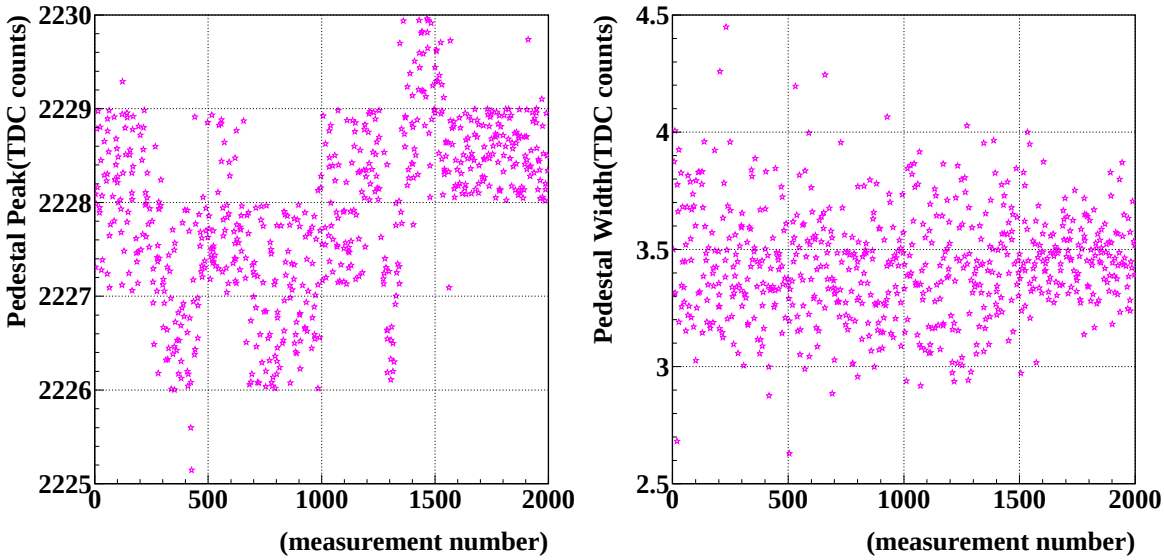

Figure 6.7: History of (a)pedestal and (b)it's width over 2 months.

6.5 Electronics Performance

6.5.1 Noise Level

Fig. 6.7 shows the history of the peak and the width of the pedestal distribution obtained by the Gaussian fitting. The horizontal axis is the time scale and the full scale corresponds to 2 months. The pedestal value was stable ($\pm$ 1 counts) over long time.

A typical distribution of the pedestal run in the low range for single channel is shown in Fig. 6.8(a). The distribution of the pedestal after summing all 36 channels are shown in Fig. 6.8(b). The width of the pedestal distribution corresponds to the electronics noise level. The electronics noise consists of the preamplifier internal noise and external pickup noise. The former is independent in each channel (incoherent) and the latter happens at the same time for all channels (coherent). From the fitting of the pedestal distribution of the single channel $\sigma_{i,0}$ and the sum of n channels σ_n, coherent noise and incoherent noise are separated using the following formula;

$$\sigma_{i,0}^2 = \sigma_{i,in}^2 + \sigma_{i,ch}^2 \tag{6.6}$$

where $\sigma_{i,in}$ and $\sigma_{i,ch}$ stand for incoherent and coherent noise component of i-th channel, respectively. The total noise is given by using σ_{in} and σ_{ch} of all channels and separated

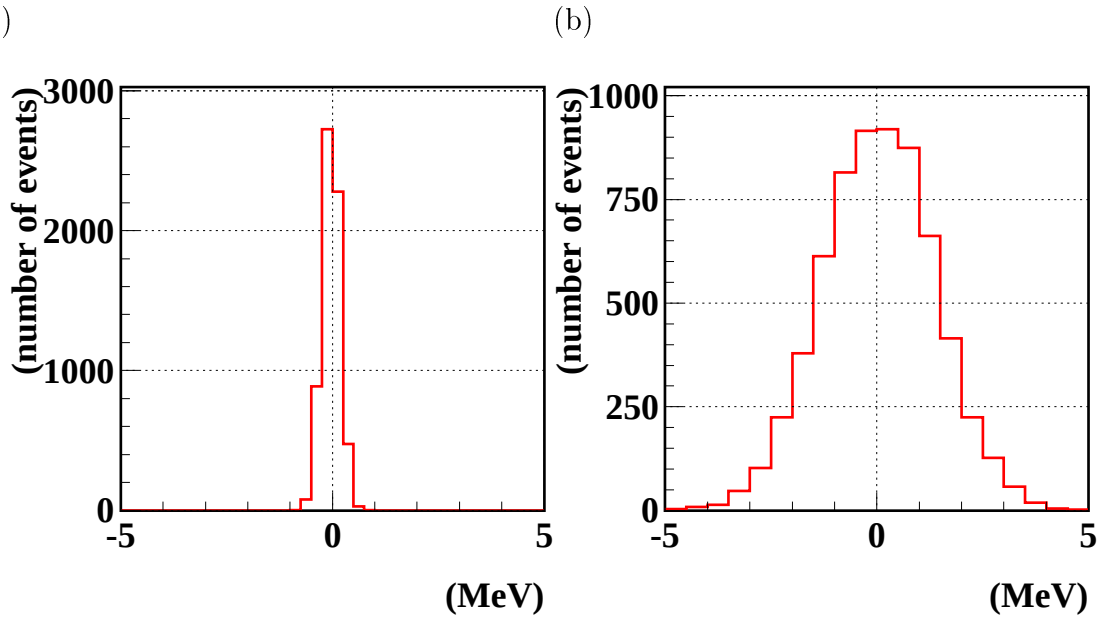

Figure 6.8: Typical pedestal distribution of (a) one channel and (b) the sum of 36 channels after conversion to energy unit.

to two components as follows;

$$\sigma_n^2 = \sum_{i=1}^{n} \sigma_{i,in}^2 + (\sum_{i=1}^{n} \sigma_{i,ch})^2 \tag{6.7}$$

$$< \sigma_{i,ch}^2 >= \frac{\sigma_n^2 - \sum_{i=1}^{n} \sigma_{i,0}^2}{n^2 - n} \tag{6.8}$$

$$< \sigma_{i,in}^2 >= \frac{(\sum_{i=1}^{n} \sigma_{i,ch})^2 - \sigma_n^2}{n^2 - n}. \tag{6.9}$$

From the above equation, the coherent and incoherent noise are calculated to 16.5 keV and 189 keV in average for n = 36 counters. They correspond to 75 and 950 electron hole-pairs in ENC.

6.5.2 Electronics Linearity

The electronics linearity is checked by a test pulse. Fig. 6.9 is an example of the results of test pulse run. The input voltage are $0 \sim 0.8$ V (corresponding to $0 \sim 1$ GeV) for MQT low range, $0 \sim 2.4$ V ($0 \sim 3$ GeV) for MQT middle range, and $0 \sim 4$ V ($0 \sim 5$ GeV) for MQT high range. The full scale in each range was equally split in 20 steps.

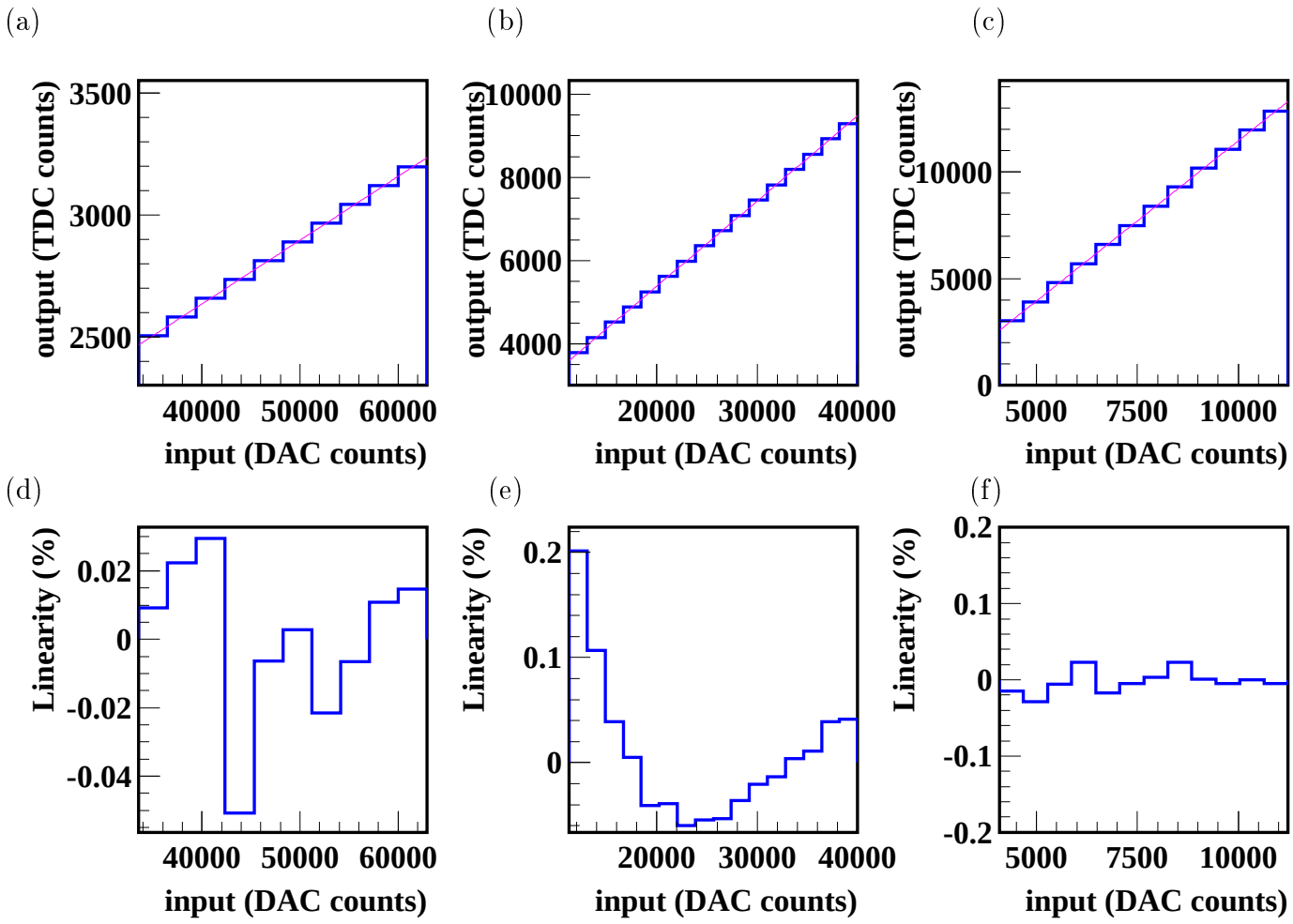

Figure 6.9: Test pulse calibration for (a) High, (b)Middle and (c)Low ranges. (d)-(f) shows the deviation from the linear fitting in % for each range.

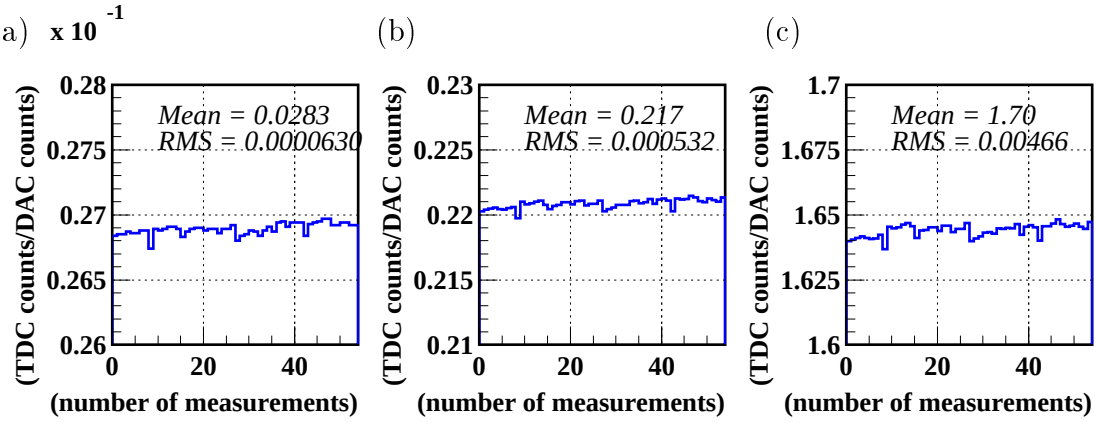

Figure 6.10: Stability of the test pulse slope in (a) High, (b)Middle and (c)Low range of MQT.

In Fig. 6.9, about 4000 DAC channels correspond to 0 V and 100 DAC channels are equivalent to 1 MeV. In each step, the peak channel was determined by the Gaussian fit and is plotted in Fig. 6.9 (a),(b) and (c).

Fig. 6.9 (d),(e) and (f) show the deviation of each point from the linear fitting line as defined bellow;

$$\frac{y_i - f(x_i)}{f(x_i) - f(x_0)} \times 100\ (\%). \tag{6.10}$$

$f(x_i)$: linear fitting function
x_i : i-th input DAC channel
x_0 : input DAC channel which corresponds to 0 V.
y_i : i-th output TDC channel

We used the low range for $0 \sim 700$ MeV and the middle range for higher than 700 MeV in the data analysis. The electronics linearity was measured for low range and it was less than 0.1% for higher energies than 10 MeV. The high range of MQT was not used. Since the electronics was proved to have a good linearity, we did not have any correction of the linearity.

6.5.3 Electronics Calibration

The output of MQT has three ranges to have a good resolution over a wide dynamic range. The ratio of slopes obtained by the test pulse run is used as the conversion factor between different ranges. The ratio was 6.98 to 7.87 between low and middle range and 7.67 to 8.32 for middle and high ranges. A long term stability of the slope

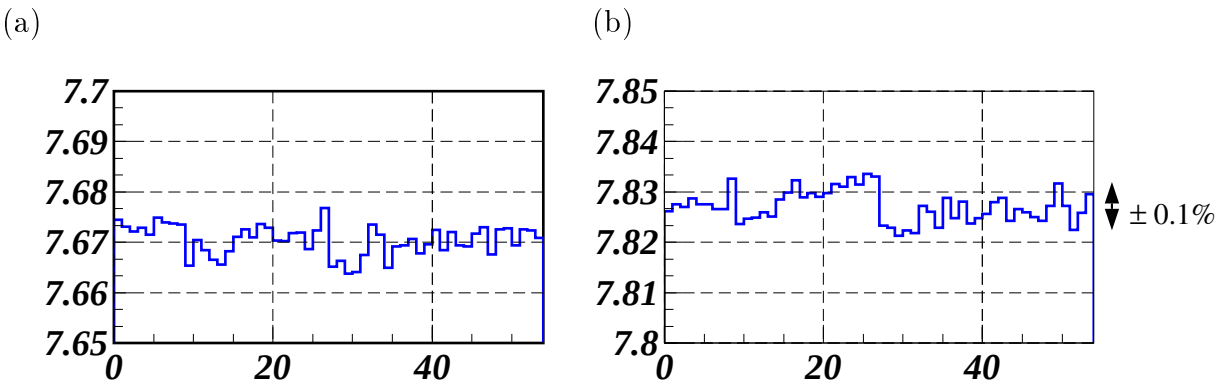

Figure 6.11: Stability of the test pulse ratio for (a)H/M and (b)M/L for a typical channel. The stability is within 0.1 %.

for a typical read out channel is shown in Fig. 6.10. The stability of the ratio is also shown in Fig. 6.11. As shown in the figures, the slope was stable within ± 0.3 % over 2 months of data taking period. The ratio was stable within ± 0.1 % for the same period.

6.6 Energy Calibration

The energy of the injected photon is calculated by the following formula for each event by summing the output of crystals in a 3 × 3 or 5 × 5 region around the central crystal.

$$E = A \times \sum_{i=1}^{9,25} (T_i^j - P_i^j) \times C_i \times R_i^j, \tag{6.11}$$

T_i^j : TDC counts of i-th counter in j-th MQT range,
P_i : Pedestal value of i-th counter in j-th MQT range,
C_i : Calibration constant of i-th counter,
R_i^j : MQT range factor,
$R_i^L \equiv a_i^L / a_i^L = 1$,
$R_i^M \equiv a_i^M / a_i^L$,
$R_i^H \equiv a_i^H / a_i^L$,
A : Overall correction factor,
a_i^j : test pulse slope of i-th counter in j-th MQT range,

where i is the index of the counter and j is the index of the MQT sensitivity range (j = L, M, H). For each counter, a most appropriate MQT range is chosen from j = L,

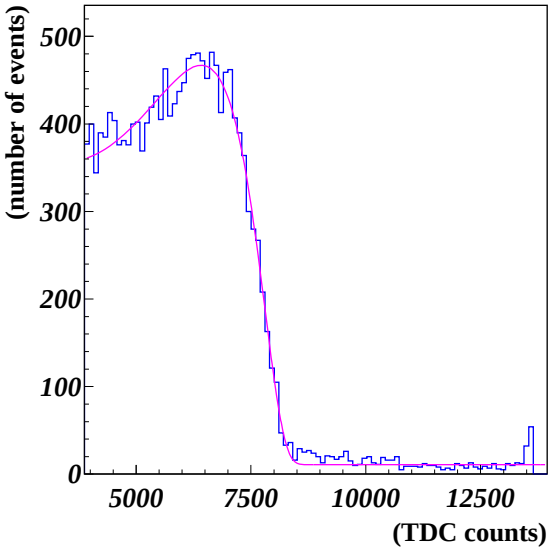

Figure 6.12: Pulse height distribution for the back scattered Compton photons for 1 counter. The theoretical Compton edge is at 508 MeV.

M, H. Such T_i^j is the TDC count of the lowest (most sensitive) range not exceeding the overflow count of the corresponding range.

In order to get the calibration constant C_i, Compton photon beam and cosmic muons were used. The calibration with the photon beam was done only once during the beam time for the central 16 counters at the center of the matrix. The cosmic-ray calibration was done once every few days for all the counters during the measurement time. Two calibration were related using the ratio of the calibration constant for the central 16 counters. The average of 36 counters by the cosmic-ray calibration was also used to correct a time dependence of the calibration.

For the cosmic-ray calibration of each counter, we selected events in which the above and below counter are both fired. This was to make sure a muon passes through the entire thickness of the counter. The track of the muon was reconstructed by the streamer tubes and the inclination of the muon track was determined. The track length inside the crystal calculated in this way has an accuracy of 1.5 %. The mean energy loss of the cosmic muon is 5.67 MeV per cm in CsI if we approximate it by a minimum ionizing particle. With this value and the path length inside the crystal for each event, we plotted the distribution of the TDC channel per MeV energy loss by the cosmic ray. The calibration constant C_i is the inverse of the peak position of this distribution. It has the unit of MeV/TDC count.

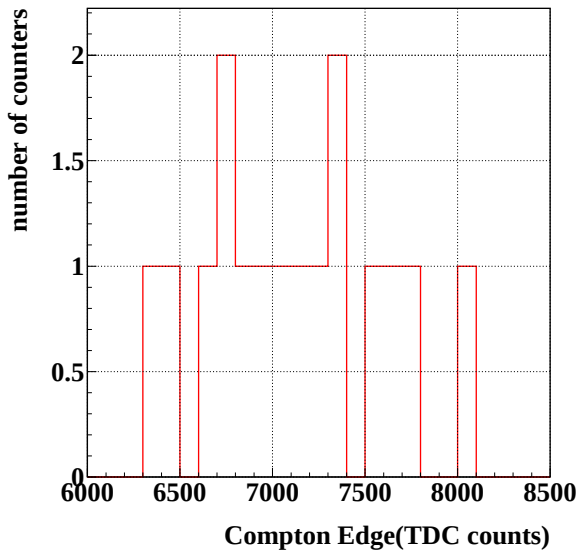

Figure 6.13: Distribution of beam calibration constants for central 16 counters.

The photon beam calibration used 4036 MeV electron beam setting. The Compton photon beam with 508 MeV maximum energy was injected at the center of each counter by adjusting the position and angle of the moving table which is supporting the crystal matrix. Due to the limitation of the moving table, twenty counters in the outer layers of the matrix were not measured by this method. An example of the low range TDC distribution after pedestal subtraction is shown in Fig. 6.12. This is the distribution for one counter at which the photon beam was aimed.F The calibration constant is obtained from the TDC edge value and calculated Compton edge energy.

Fitting function used is the same as that used in the normal Compton run which will be explained in APPENDIX C. The fitting was done in 2 steps to obtain a stable fitting result. In the first fitting, the TDC channels corresponding to the Compton edge and asymmetry parameter η are determined for each counter. In the second step, the fitting region is limited to 50 $\sim$ 180 % of the Compton edge and the asymmetry parameter was fixed as the average of 16 counters obtained in the first step. The distribution of the fitted Compton edge which is proportional to the inverse of the calibration constant C_i, is shown in Fig. 6.13. In order for two sets of calibrations to be consistent, we multiplied all the photon beam calibration constants by a constant S ($\equiv$ average of C_i obtained by cosmic rays / average of C_i obtained by photon beam).

Fig. 6.14 shows the comparison between the scaled beam calibration constant and

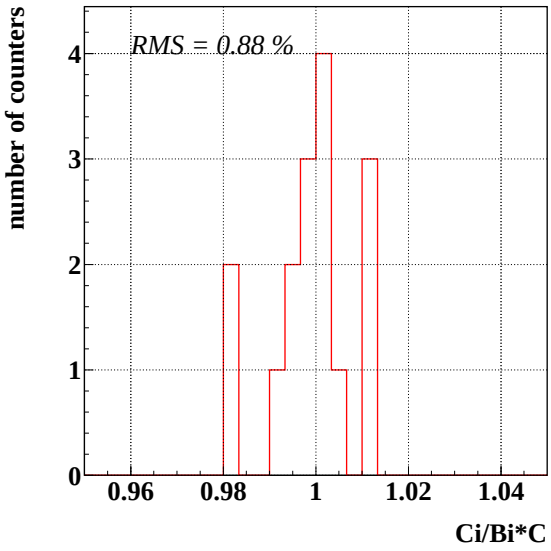

Figure 6.14: Ratio of the cosmic-ray calibration to the beam calibration.

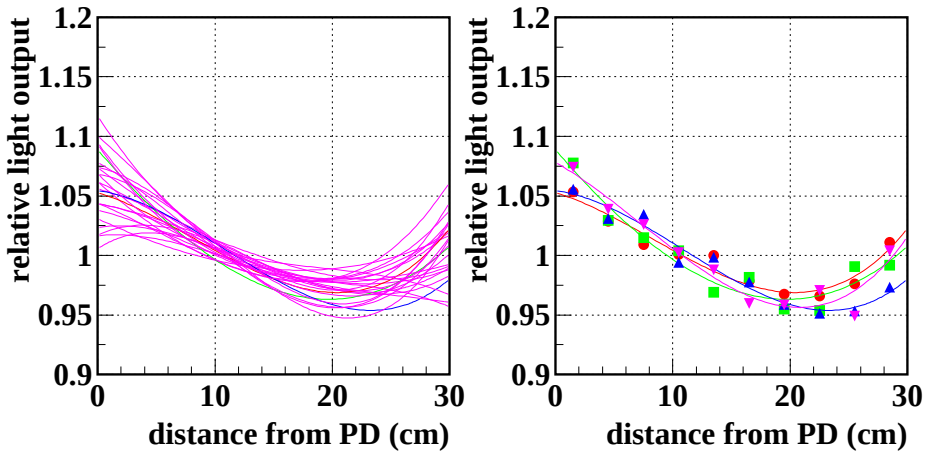

Figure 6.15: Position dependence of the light output measured by cosmic rays for (a) all counters and (b) central four counters after scaling to the average light output of each counter.

the original cosmic-ray calibration constant for the central 16 counters. Both of beam calibration and cosmic-ray calibration are consistent within a rms of 0.88 %. For the subsequent analysis of energy resolution and linearity, we use the scaled photon beam calibration for the central 16 counters and the original cosmic-ray calibration constants for the outer 20 crystals. The gain variation of 36 different electronics channels, which amounts to ± 10 % at maximum, are automatically corrected in this process.

In order to determine the value of correction factor A, the effect of longitudinal non-uniformity has to be considered carefully. The position dependence of the cosmic ray pulse height is shown in Fig. 6.15. The light output is higher near the photodiode and the behavior is similar for all the counters. On the other hand, the energy deposit by the photon is heavily weighted at the front part of the crystal. Fig. 6.16 shows the energy deposit in each 3 cm slice of the CsI crystal obtained by GEANT simulation when the Compton photon beam of 508 MeV is injected from the front face of the crystal. It is clear from the figure that the most of the energy is deposited in the first half of the crystal which has the lower light output.

The cosmic-ray calibration constants are calculated as the average of all subparts and the effect of non-uniform energy deposit by the photon is not included. In order to correct that effect, GEANT simulation was done for the Compton photon beam. The non-uniformity function used in GEANT is described later in section 6.7.7. We made four Monte Carlo simulations by injecting the 508 MeV Compton photon beam at the center of one of the (3,3)(3,4)(4,3)(4,4) crystals. The fitted Compton edge of 5 × 5 counters was 497.0 MeV for the Monte Carlo contrary to the Compton edge of 508 MeV. The value of 497.0 MeV is the estimate of energy deposit by the Monte Carlo with shower leakage taken into account. We determined the value of A such that the 5 × 5 energy deposit calculated by the formula (6.11) for data gives the same edge value of 497.0 as the Monte Carlo simulation. We found the value of $A = 1.021$ and the absolute energy scale given by the cosmic-ray calibration seems fairly accurate.

We used only one set of C_i described above to analyze all the data taken over 2 months of beam period. But a small time dependent factor is applied on C_i. Fig. 6.17 shows the history of the temperature of the crystal and electronics together with the relative shift of cosmic-ray calibration constant averaged over 36 counters. The correlation between two parameters indicates that the light output of CsI crystal is affected by the temperature and this is to be corrected. We used this relative shift to represent the variation of C_i with temperature. In the analysis of the data, we took the correction from the most nearby cosmic-ray calibration in time. The maximum of this correction was 0.8 %.

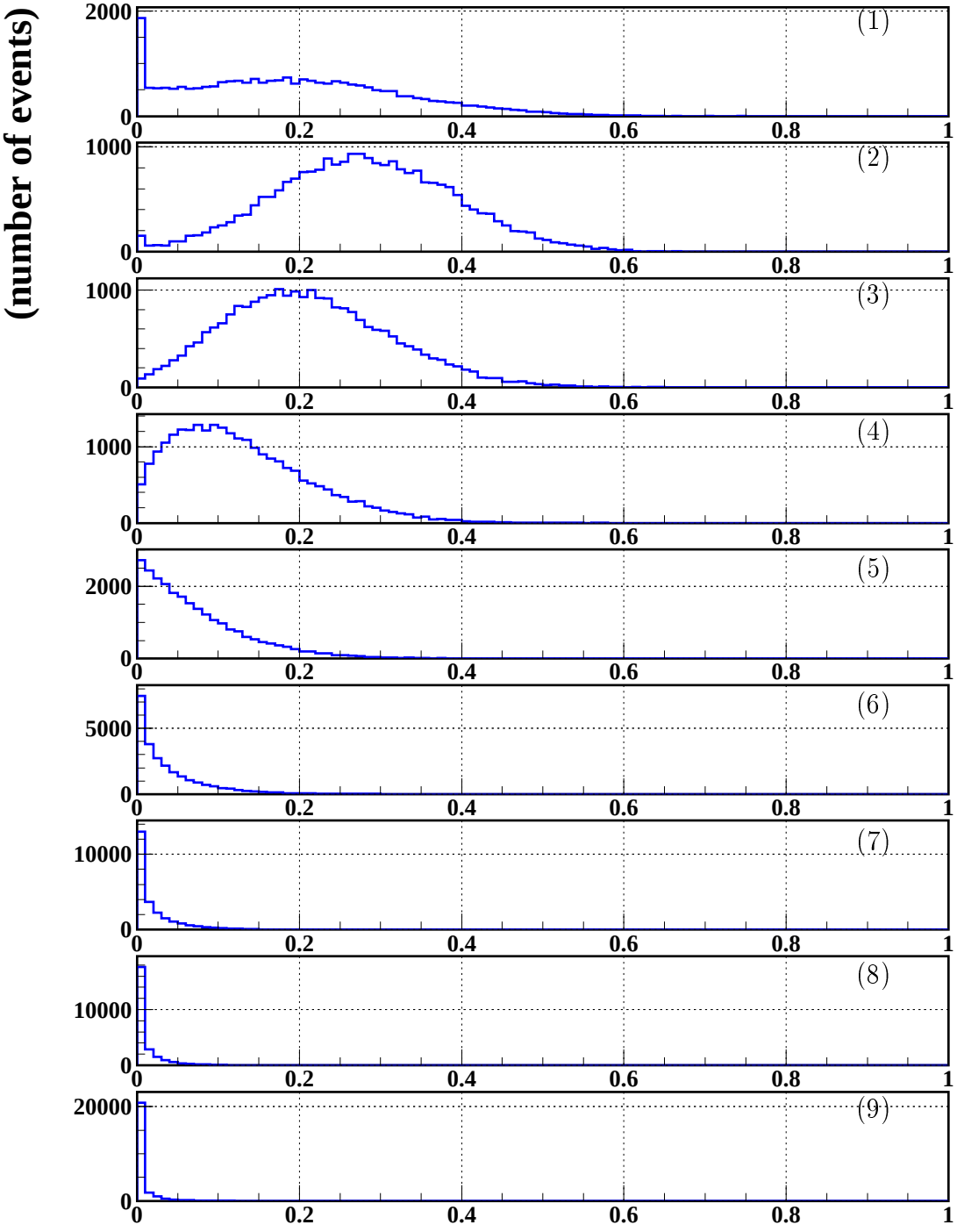

Figure 6.16: Energy deposit in longitudinal slices of the CsI(Tℓ) crystal for 508 MeV Compton beam. The depth of each slice is 3 cm.

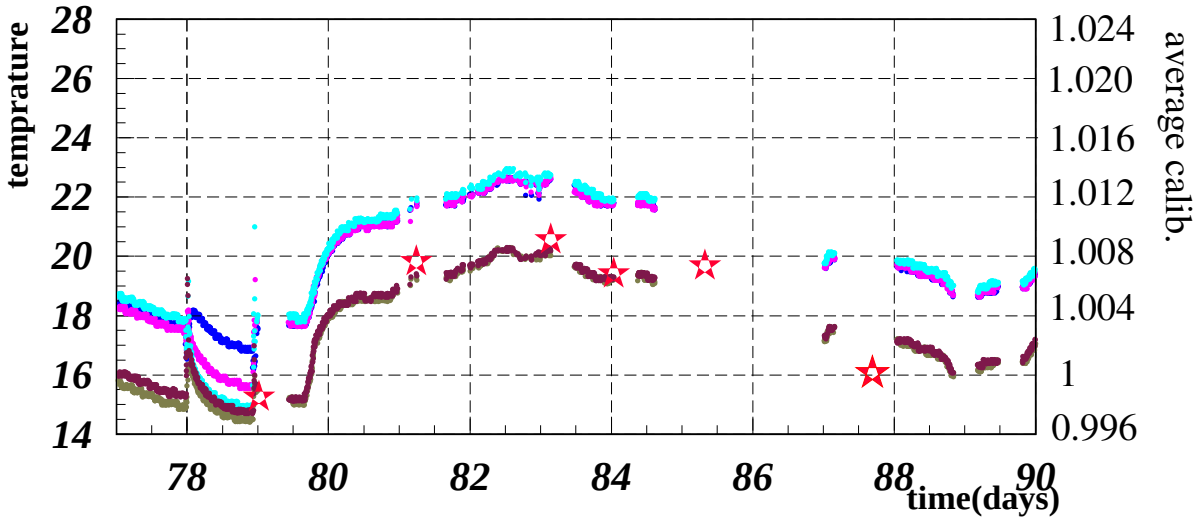

Figure 6.17: Temperature dependence of cosmic-ray calibration. Lines indicate the temperature at several locations in the data taking room, and stars are the average of the cosmic-ray calibrations of 36 counters.

6.7 Energy Resolution

6.7.1 Tagged Photon Analysis

There are two methods to get the energy resolution of the CsI(Tℓ) counter from Compton photon beam. The first method uses the tagging system (TS) to estimate the photon beam energy event by event. Fig. 6.18(a) shows the correlation between the energy obtained by CsI counters (E_{CsI}) and by the tagging system (E_{tag}). Using the tagged photon energy, the energy dependence of the energy resolution can be studied from the lowest limit of the tagging system acceptance up to the Compton edge. We divided the whole energy range of E_{tag} into several subparts and plot the ratio of E_{CsI} and E_{tag} in each subpart. Fig. 6.18(b) shows a typical distribution of the ratio $R_E \equiv E_{CsI}/E_{tag}$ together with the fitting function of a logarithmic Gaussian. The upper and lower tail regions of R_E with histogram contents below 20 % of the peak value were removed from the fitting to suppress the uncertainty in the fitting procedure. For this method, the resolution of E_{CsI} is obtained by subtracting the resolution of E_{tag} from the resolution of R_E in quadrature as follows,

$$\sigma_{E_{CsI}} = \sqrt{\sigma^2_{R_E} - \sigma^2_{E_{tag}}}. \tag{6.12}$$

(a) (b)

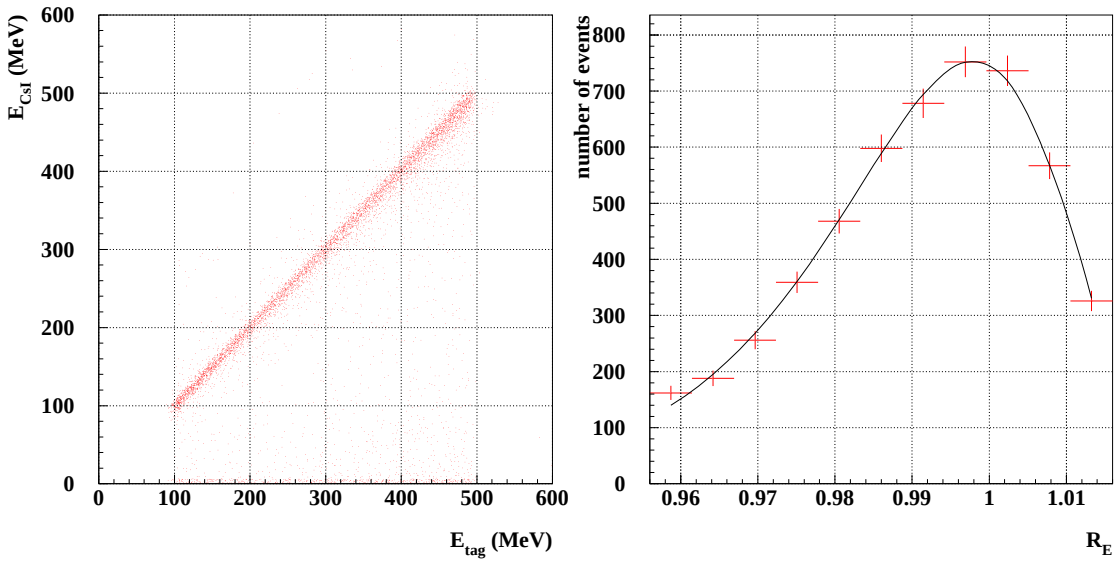

Figure 6.18: (a)Correlation between the energies E_{CsI} and E_{tag} for 508 MeV Compton run. (b)Distribution of R_E with fitting . The fitting region is 410 $\sim$ 510 MeV.

6.7.2 Compton Edge

The second method is the fitting of the shape of the Compton edge. The convolution of Compton spectrum (6.1) and the resolution function (5.1) is used for the fitting (APPENDIX C). The examples of the fitting is shown in Fig. 6.19. To avoid the systematic shift of the fitting results by the different fitting region, the fitting was done in two steps. An approximate position of the edge E_{edge} and the resolution σ_E were determined in the first step. The fitting region was limited to [$E_{edge} \pm 5\sigma_E$] in the second step.

The fitting function includes a background term coming from the overlapping of two Compton photons in a single laser pulse. The distribution of the background was analyzed by Monte Carlo simulation. If 20 % of the event has a contribution from the second photon, the energy spectrum looks like Fig. 6.20. From the figure, the background distribution of triangular shape in the fitting function is justified.

6.7.3 Bremsstrahlung Edge

The Bremsstrahlung photon spectrum edge also used for the estimation of the energy resolution using the same way as used for the Compton spectrum edge. The fitting

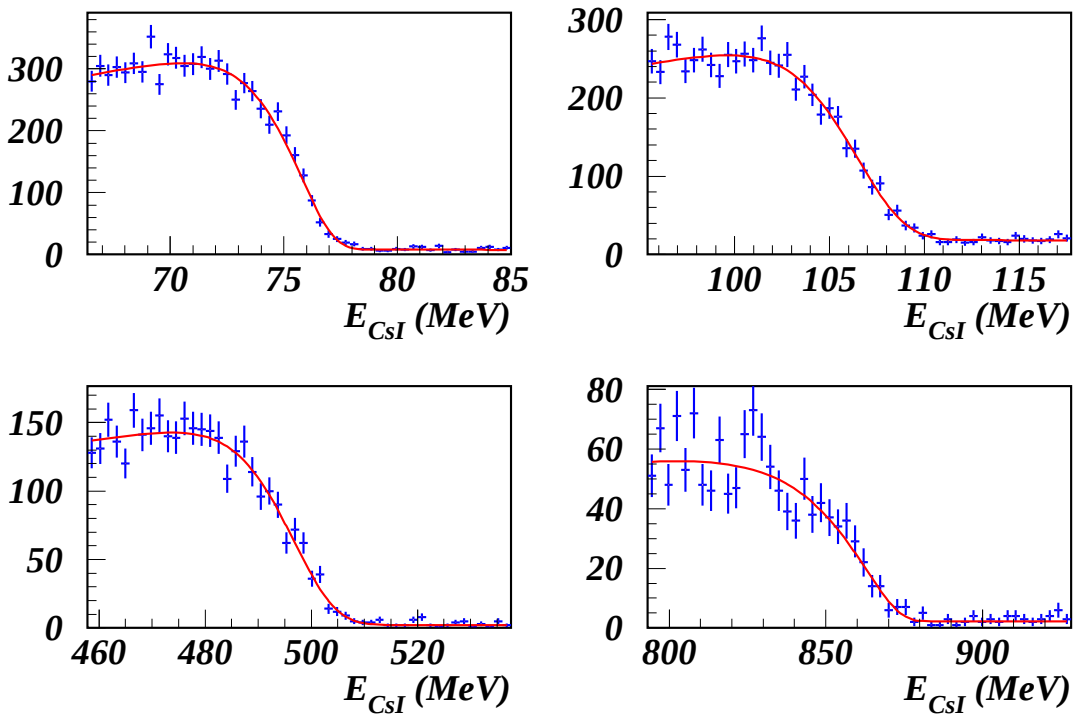

Figure 6.19: Typical Compton edge distributions. The solid line in each figure is the fitting results.

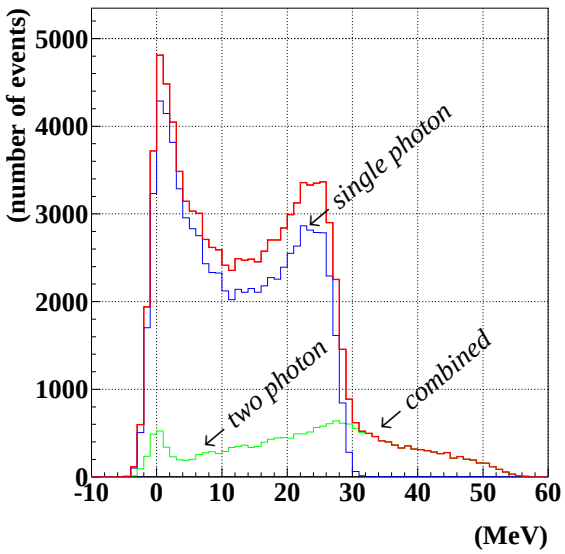

Figure 6.20: Compton photon distribution with two photon background by Monte Carlo simulation. The percentage of 2 photon is 20 % of the single photon.

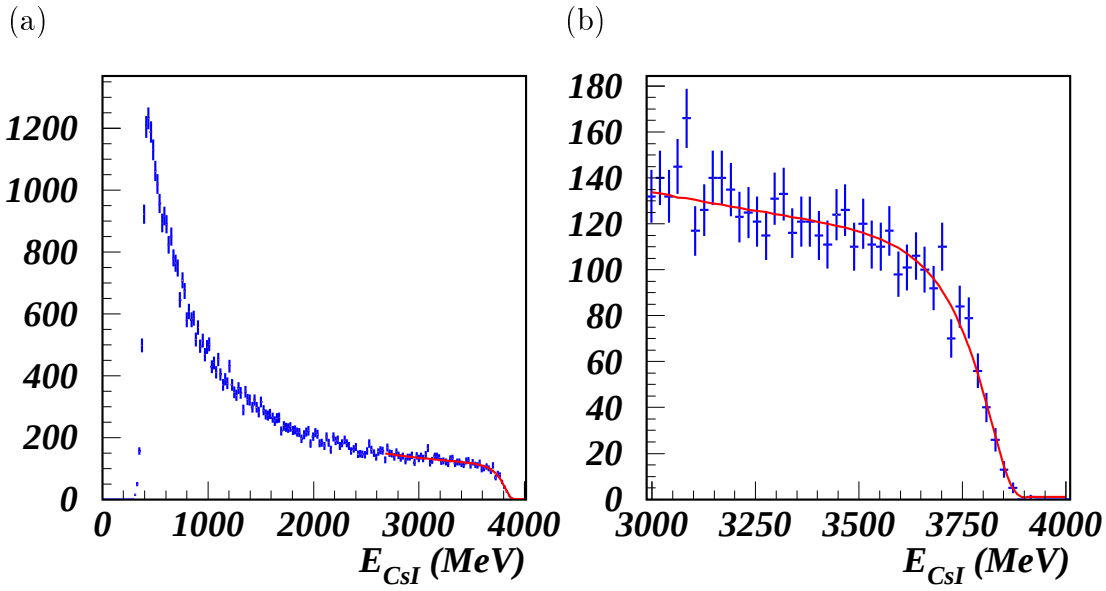

Figure 6.21: (a)Typical Bremsstrahlung distribution for 4036 MeV electron beam and (b)the expanded view of the edge region with fitting result.

function is the convolution of the theoretical Bremsstrahlung function and the CsI response function. The distribution is shown in Fig. 6.21. Fitting region is taken from 67 % to 100 % of the incident electron beam energy.

6.7.4 Asymmetry Parameter

For all three methods, the asymmetry parameter η of the fitting function affects the estimate of the resolution. Both of the edge fittings need special care because the asymmetry parameter tends to be unstable in the fitting. In Fig. 6.22, we show the energy dependence of the asymmetry parameter η obtained from the fitting of the R_E. In fitting the Compton and Bremsstrahlung edges, we fixed the asymmetry parameter η at the values represented by the solid curve in Fig. 6.22.

6.7.5 Energy Resolution for Simple Sum

The result of the energy resolution for a simple sum is shown in Fig. 6.23(a)(b) for the 3×3 and 5×5 matrix, respectively. The simple sum means the sum of all signals from the 3×3 or 5×5 crystals around the beam injected crystal. The solid line shows the tagging system resolution which is quadratically subtracted from the resolution of R_E.

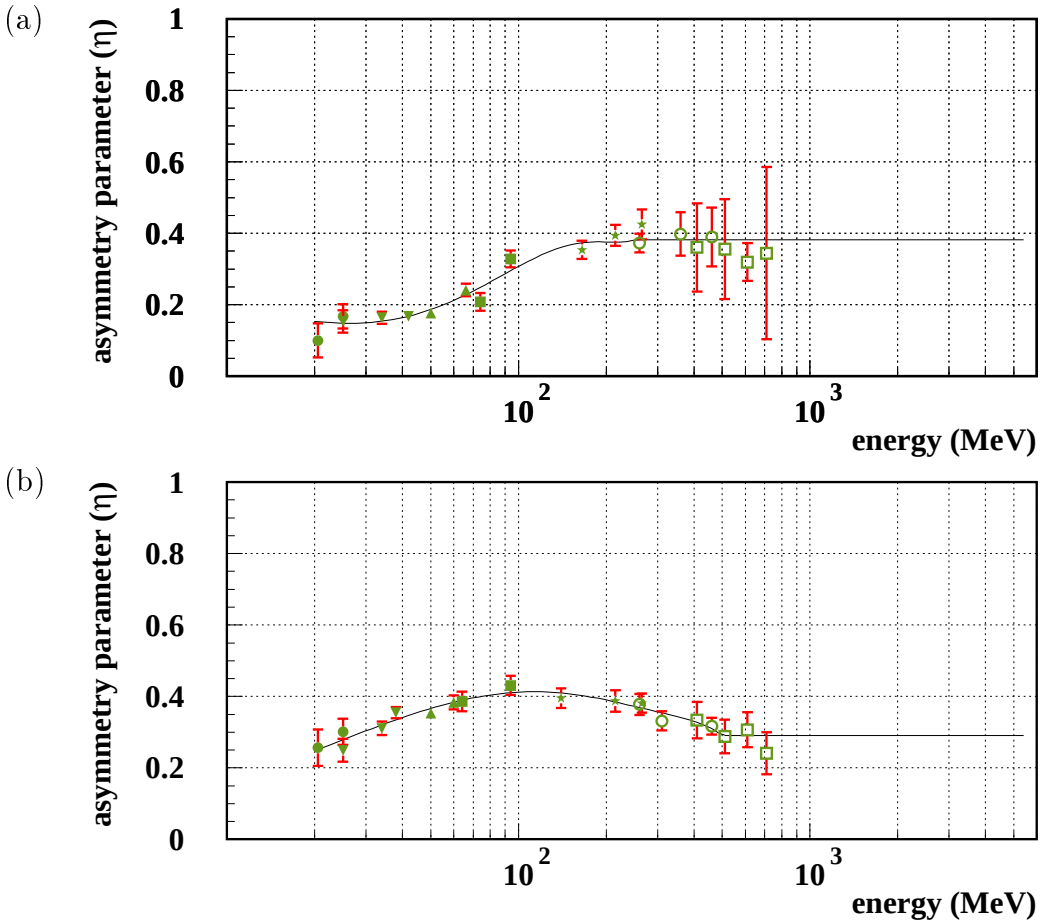

Figure 6.22: Energy dependence of asymmetry parameter η obtained from the fitting of R_E for (a)5x5 and (b)3x3 matrix with fitting.

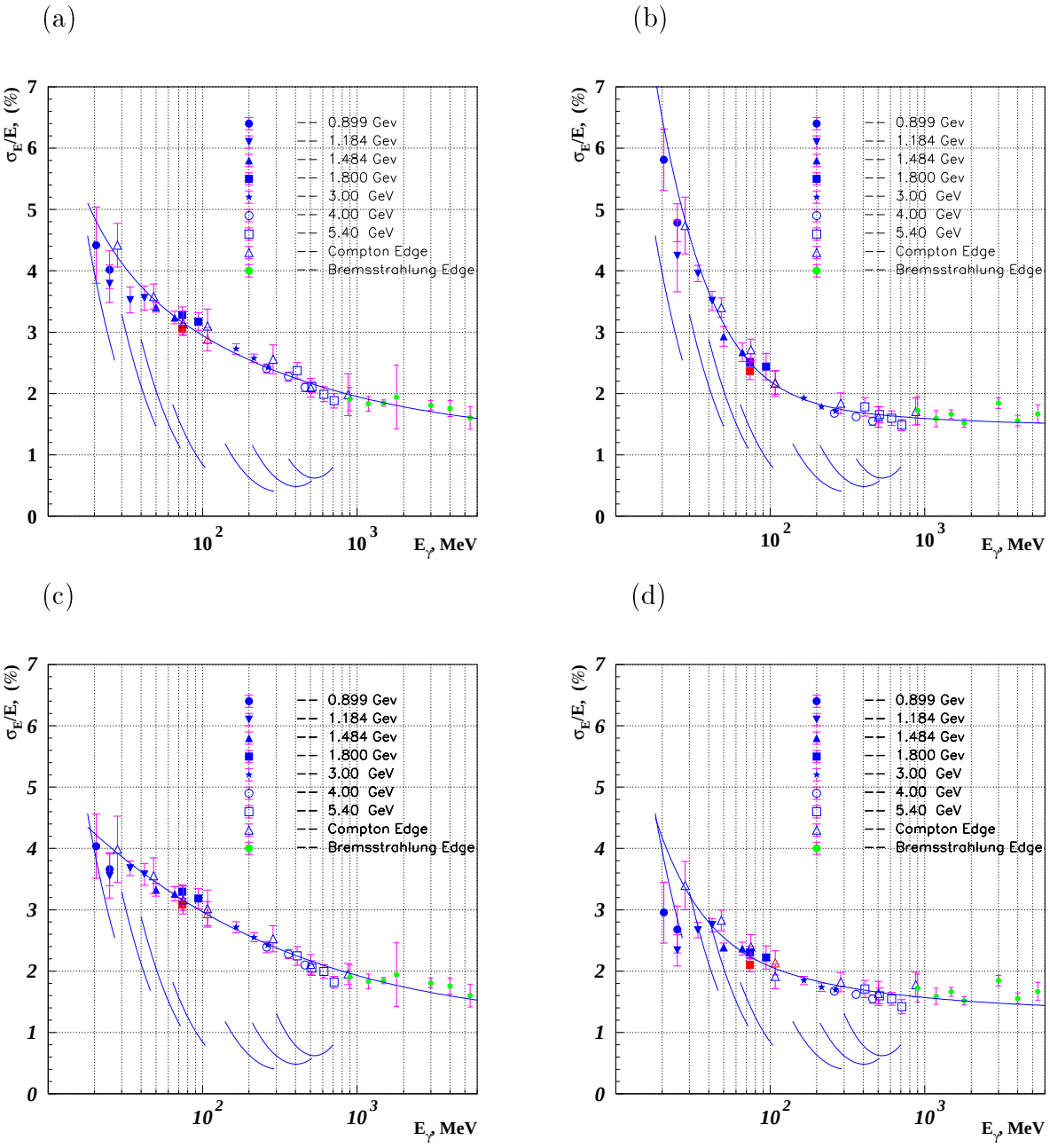

Figure 6.23: Energy resolution as a function of incident photon energy for (a)3 × 3 and (b) 5 × 5 matrix by the simple sum. The energy resolution of (c)3 × 3 and (d)5 × 5 matrix with the threshold of 0.5 MeV. Solid lines are results of the fitting. The resolution of the tagging system is given in seven separate lines below the data points.

The resolutions obtained by three methods (i.e. R_E, Compton edge, Bremsstrahlung edge analysis) are in good agreement each other for an energy range from 20 MeV to 5.4 GeV. The result of 3×3 matrix is better than 5×5 in the region below 40 MeV where the electronics noise makes a dominant contribution to the resolution.

The resolution can be fitted by the quadratic sum ($\oplus$) of the following three terms. The first term is from the contribution of electronics noise, the second term and a part of the third term represent the shower leakage fluctuation and the third term also includes the systematic effects such as the calibration uncertainty of the crystals.

The results are

$$\frac{\sigma_E}{E} = \frac{0.053(\%)}{E} \oplus \frac{1.46(\%)}{E^{1/4}} \oplus 1.30(\%), \quad E \text{ in GeV} \tag{6.13}$$

for 3×3 matrix and

$$\frac{\sigma_E}{E} = \frac{0.127(\%)}{E} \oplus \frac{0.55(\%)}{E^{1/4}} \oplus 1.47(\%), \quad E \text{ in GeV} \tag{6.14}$$

for 5×5 matrix.

The solid lines in Fig. 6.23 are the results of the fitting.

6.7.6 Energy Resolution with Threshold

Fig. 6.24 shows the number of counters which have the energy deposit greater than certain threshold value in 5×5 matrix. The number depends on the incident photon energy. We note that the number of counters with significant energy deposits is much less than 25 at low energy. We expect the energy resolution at low energy improves if we remove counters with no significant energy deposit.

Fig. 6.25 shows the energy resolution v.s. number of summed counters for several energy points. All the energy deposits in 5×5 matrix are arranged in energy decreasing order and only the first n counters were used for the summation of energies.

As seen in Fig. 6.25, the energy resolution for low energy photon starts deteriorating with more number of counters because the electronics noise effect goes up when the number of summed counters increase. The contribution of electronics noise is small above 100 MeV. When we limit the number of summed crystals to less than 10, the resolution is worse again due to the leakage of the shower.

In order to determine the optimum threshold for selecting the counters to be added, we plotted the threshold dependence of the energy resolution in Fig. 6.26. The best resolution is obtained at around 0.5 MeV.

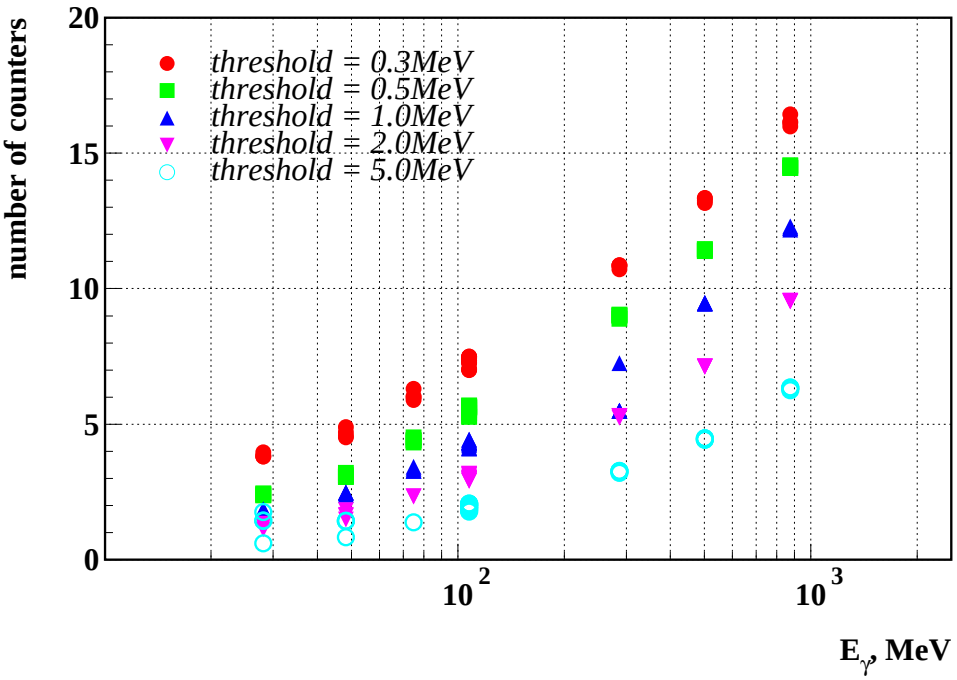

Figure 6.24: Most probable number of counters with energy deposit greater than the threshold.

The energy resolution of 3 × 3 and 5× 5 matrix obtained with the threshold of 0.5 MeV is shown in Fig. 6.23(c)(d) together with the fitting result in solid line. The result of fitting is

$$\frac{\sigma}{E} = \frac{0.0066(\%)}{E} \oplus \frac{1.53(\%)}{E^{1/4}} \oplus 1.18(\%), \quad E \text{ in GeV} \tag{6.15}$$

for 3 × 3 matrix and

$$\frac{\sigma}{E} = \frac{0.066(\%)}{E} \oplus \frac{0.81(\%)}{E^{1/4}} \oplus 1.34(\%), \quad E \text{ in GeV} \tag{6.16}$$

for 5 × 5 matrix.

The contribution of electronics noise and the resolution decreased as expected.

6.7.7 Comparison with Monte Carlo Simulation

The Monte Carlo simulation was done using GEANT program package. CsI crystals are piled up in 6 × 6 matrix as in the real experimental setup. The wrapping material of the crystal and 0.5 mm thick aluminum sheet in between crystals are also included.

The Compton photon beam is generated with the energy distribution described in

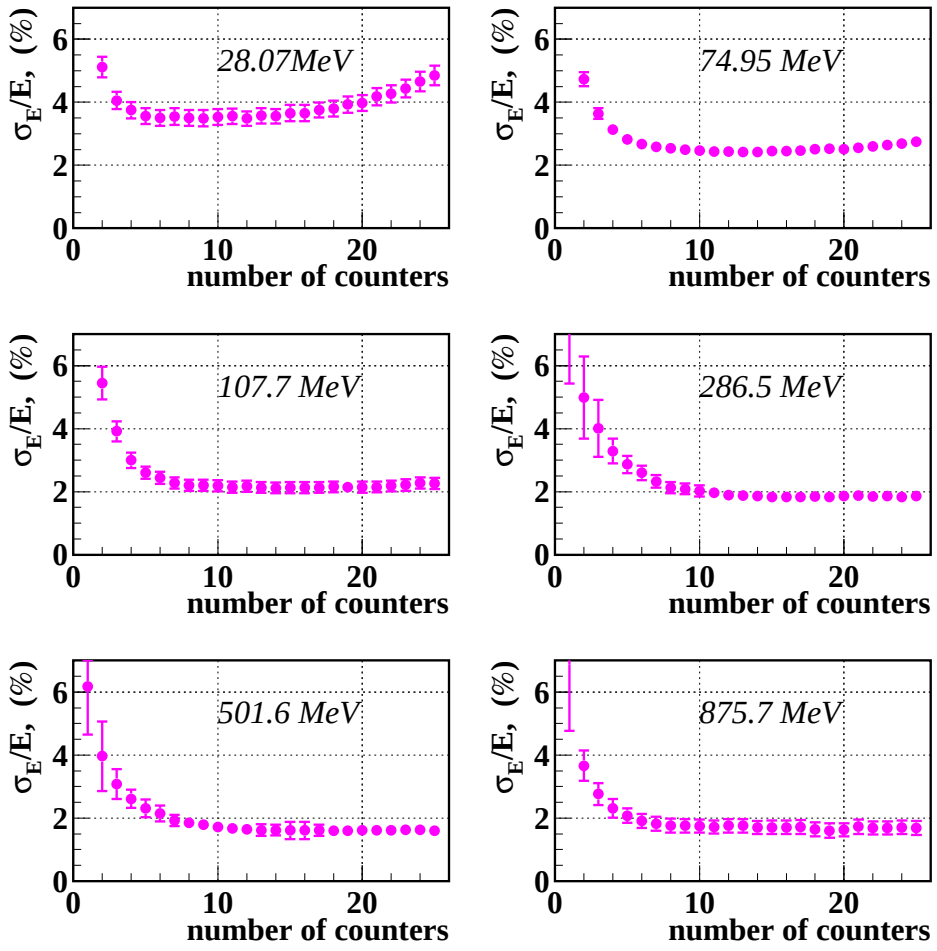

Figure 6.25: Number of counters used in the summation of energy vs energy resolution.

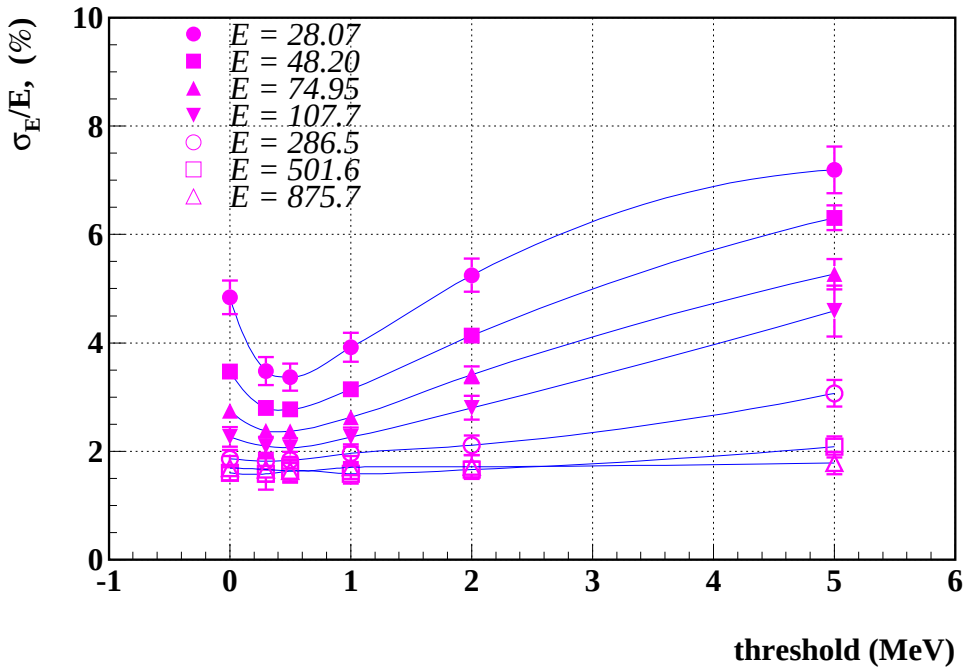

Figure 6.26: Threshold dependence of the energy resolution.

(6.1). For the Bremsstrahlung beam, monochromatic photons with energy corresponding to the Bremsstrahlung edge are used.

The spread of the beam at the matrix front face was simulated with the following formula (6.17), (6.18) with $S_x = 1$ cm, $S_y = 1$ cm for both Compton and Bremsstrahlung runs. All the photons were injected normal to the matrix front face with no angular spread.

$$f(x) = \frac{1}{1 + (\frac{x - x_0}{S_x})^2}. \tag{6.17}$$

$$f(y) = \frac{1}{1 + (\frac{y - y_0}{S_y})^2}. \tag{6.18}$$

x_0, y_0 : peak of the fitting
S_x, S_y: width of the fitting

The photon and electron in the shower was tracked down to 10 keV[‡]. Every energy deposit in each tracking step was weighted by the non-uniformity function obtained by the cosmic ray calibration. The 3rd order polynomial function was used to represent the measured non-uniformity. After summing all the energy deposits in one crystal,

[‡]CUTGAM = CUTELE = 10 keV in GEANT parameter.

smearing by the incoherent electronics noise of 189 keV and the coherent noise of 16.5 keV was added.

In order to correct the energy shift caused by the arbitrary scale of non-uniformity, the energy deposit is simulated without non-uniformity. The simulated Compton edge of the perfectly uniform crystal is 489.4 MeV in 5×5 sum for 502 MeV Compton beam. When the original scale of the non-uniformity is used, the Compton edge became 480.6, 476.9, 476.3, 477.7 MeV for the central four counters. We multiplied the uniformity function by 1.024 such that the average of four Monte Carlo simulations becomes equal to the uniform simulation result.

The distribution of the beam incident position for the Compton beam is shown in Fig. 6.27 for the data and Monte Carlo simulation. The scatter plot shows the X position v.s. Y position of the beam calculated by the center of gravity method by the following equation.

$$X_c = \frac{\sum_{i=1}^{36} X_i E_i}{\sum_{i=1}^{36} E_i}, \tag{6.19}$$

$$Y_c = \frac{\sum_{i=1}^{36} Y_i E_i}{\sum_{i=1}^{36} E_i}. \tag{6.20}$$

where X_i and Y_i are coordinate of the center of the i-th counter and E_i is the energy deposit in the i-th counter.

The histograms are the distributions of X_c and Y_c with fitting results. In the Monte Carlo, X_c and Y_c became similar value.

Fig. 6.28 and Fig. 6.29 show the comparison between the real data and the simulation result on R_E and the Compton spectrum, respectively for various energy of photons. Inefficiency of the lower part of real data are caused by the trigger threshold in STM module and the acceptance of the TS trigger counter. The data are well reproduced by the simulation for all the distributions.

Fig. 6.30 show the results of the Monte Carlo on the energy resolution. For the R_E analysis in Monte Carlo simulation, the energy deposit in CsI crystal was calculated at first. The TS resolution generated by Gaussian was then added to the 3×3 and 5×5 sum. After the fitting of R_E, the TS resolution was subtracted quadratically in the same way as for the data. The results of the simulation are consistent with the data.

In order to make a clear comparison, Fig. 6.31 shows the overlay of the data and simulation for the resolution of 5×5 sum with 0.5 MeV threshold. In the figure, the dot with error bar reproduces the real data plotted in Fig. 6.23(d) and the solid line shows the fitting result of simulation shown in Fig. 6.30(d). They are in excellent

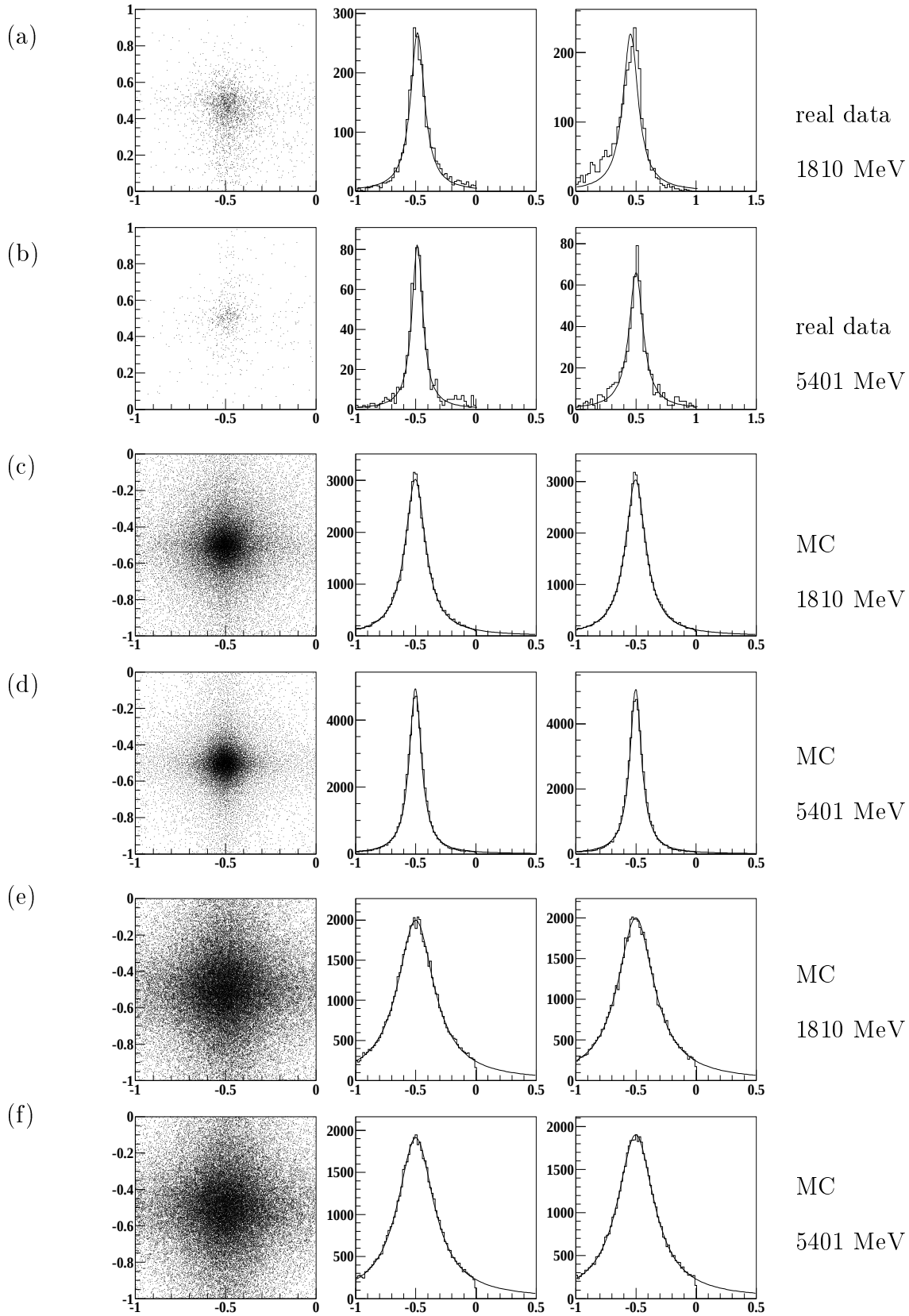

Figure 6.27: Position of beam injection point by the center of gravity method for (a)(c)1810.MeV (b)(d)5441.MeV. (a)(b) are data and (c)(d) are Monte Carlo simulation (MC) results. (e)(f) are the real beam injected points in MC. Left figures show X_c vs Y_c , middle figures show X_c distribution and right figures show Y_c distribution. The unit is the edge length of one crystal.

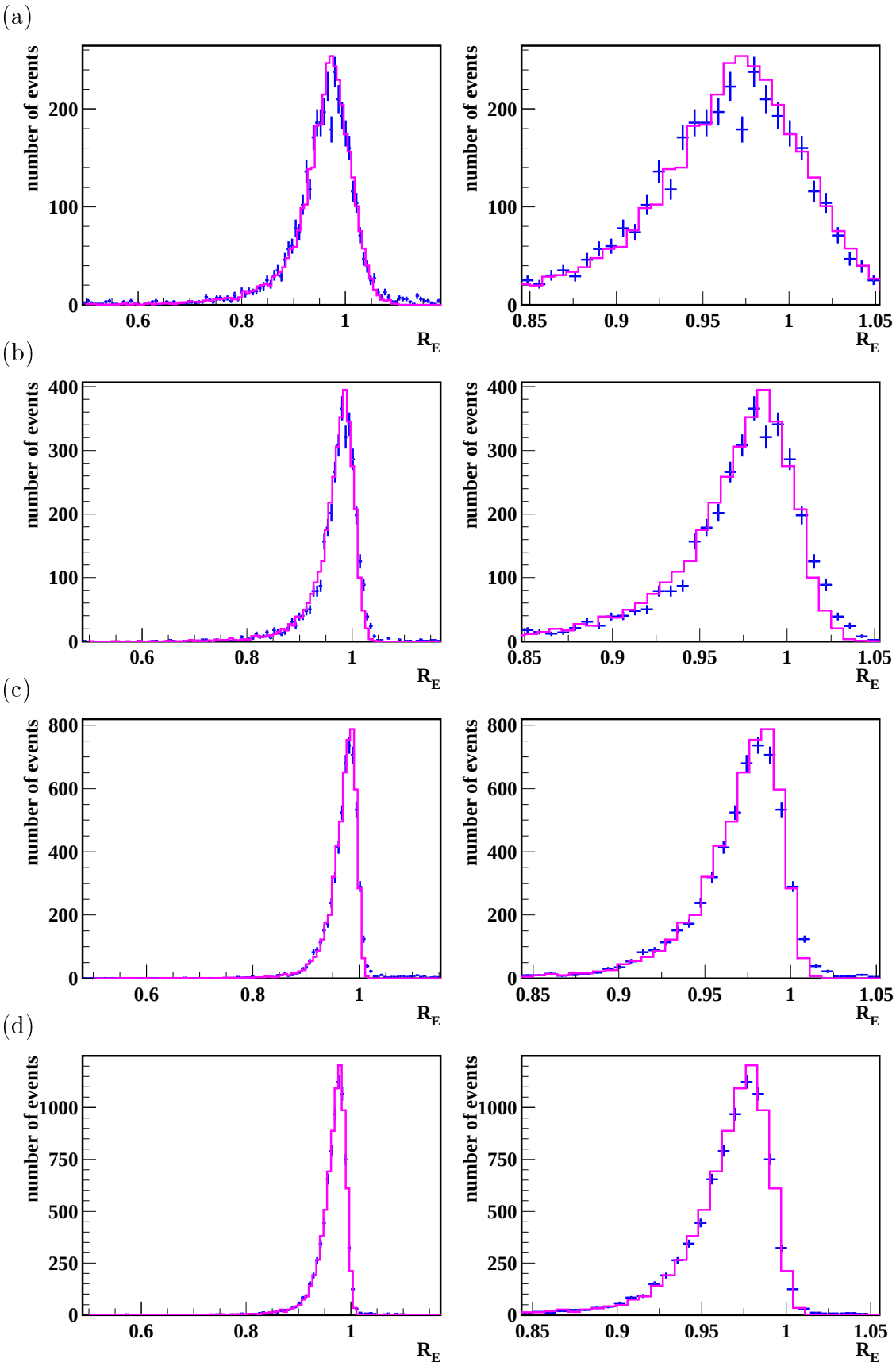

Figure 6.28: Comparison between data (cross) and simulation (histogram) of the R_E distribution for (a)27.5, (b)75, (c)300 and (d)500 MeV photon. The right figures are expanded view near the peak.

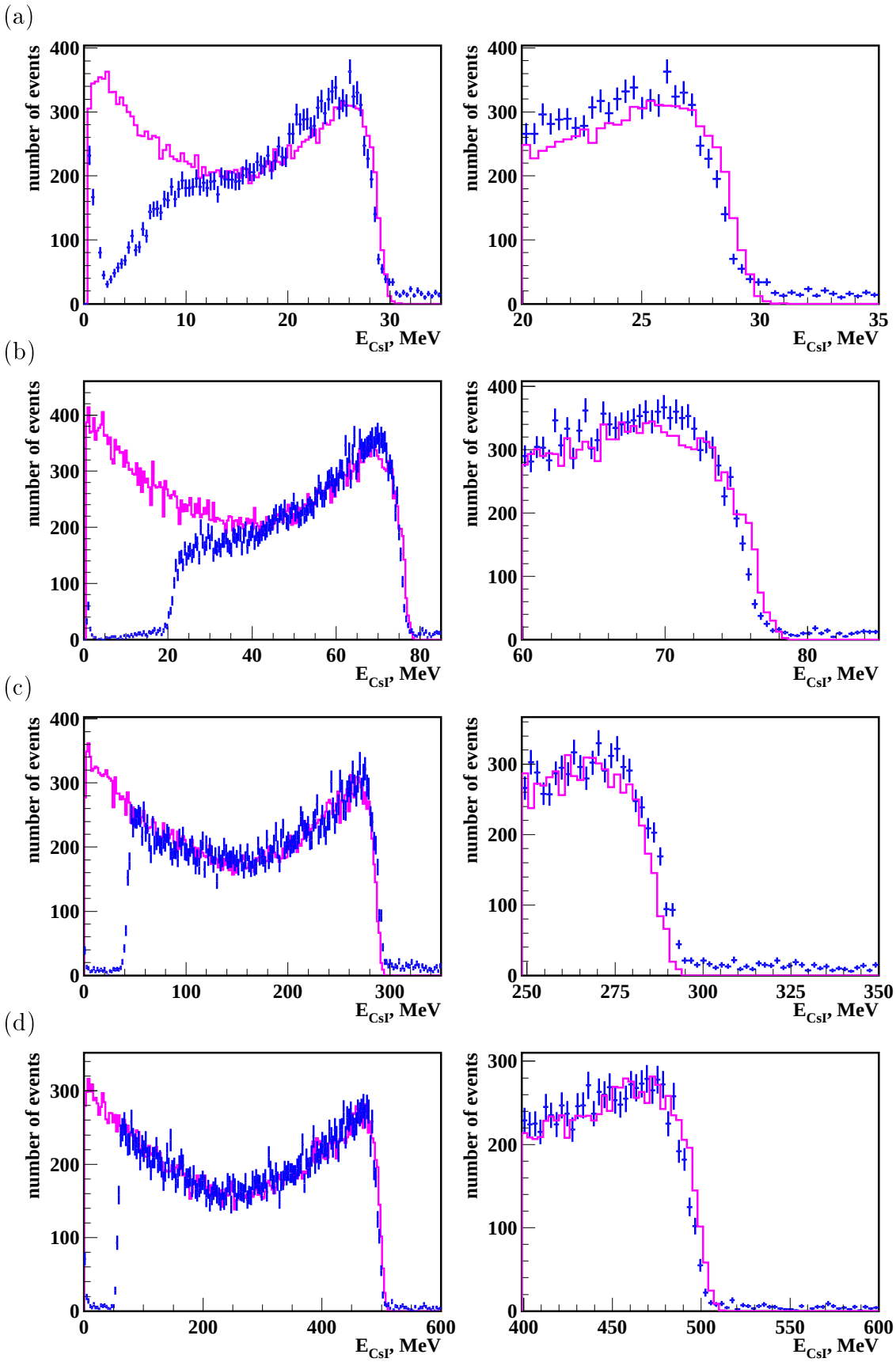

Figure 6.29: Comparison between real data (cross) and simulation(histogram) of the Compton edge of (a)29.4, (b)76.8, (c)291.5 and (d)508.3 MeV. The right figures are expanded view of the edge part.

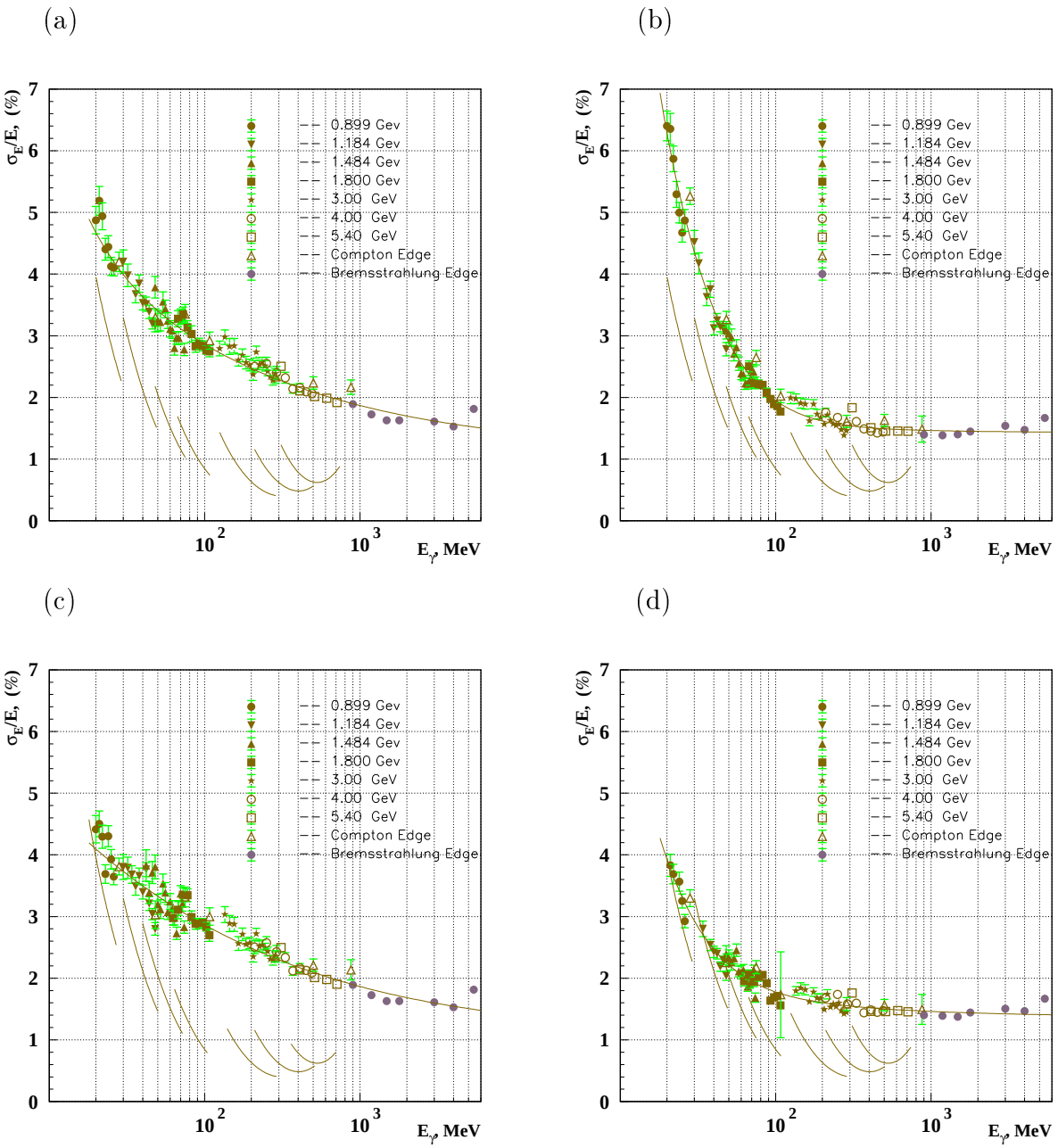

Figure 6.30: Monte Carlo simulation (MC) results of energy resolution of (a)3 × 3 and (b)5 × 5 counters, and energy resolution of (c) 3 × 3 and (d) 5 × 5 with threshold = 0.5MeV. Tagging System resolution which are drawn by solid line is included in MC and subtracted after fitting.

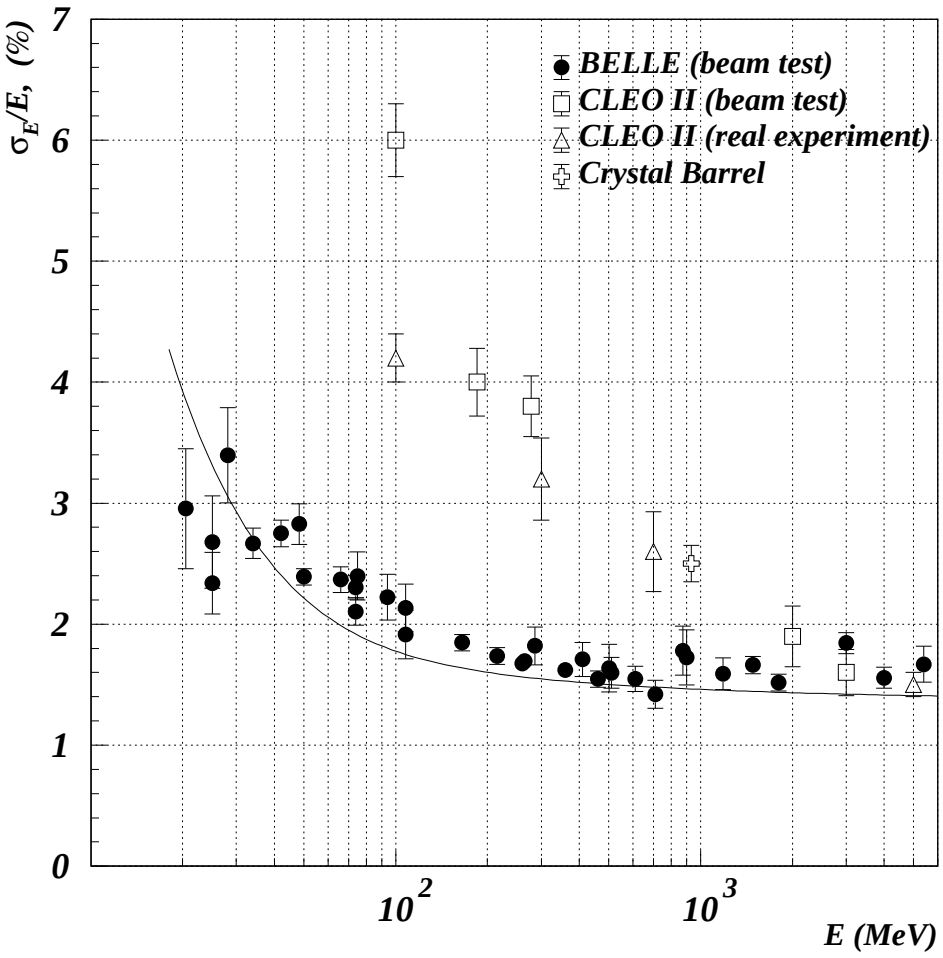

Figure 6.31: Energy resolution of 5 × 5 matrix with threshold of 0.5 MeV. The solid line is the fitting to the Monte Carlo resolution (see Fig. 6.30d). CLEO II beamtest results are obtained for 3 × 3 matrix.

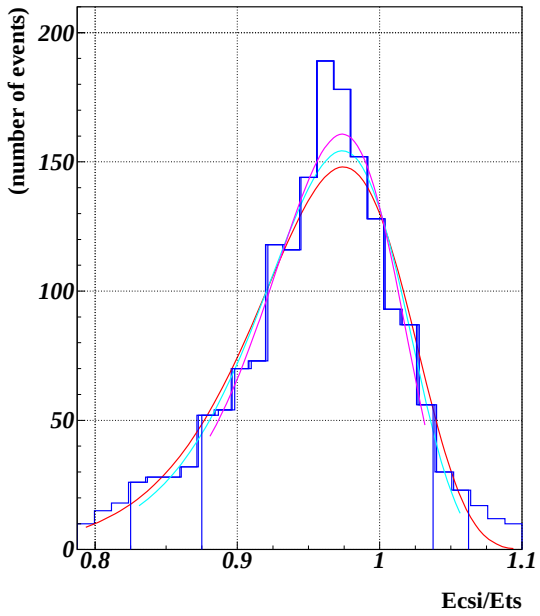

Figure 6.32: R_E distribution with different fitting regions for $E_\gamma = 25$ MeV. Different fitting regions correspond to removing histogram bins less than 5, 10, 20 % of the peak bin.

agreement. The results from CLEO and Crystal Barrel are also plotted for comparison [67] [68] [69].

6.7.8 Error in Resolution

The statistical error given by the fitting program MINUIT is at the level of 0.1 % and negligible for most of the results.

For the tagged photon analysis, the resolution of TS used for the subtraction is estimated from the expected accelerator parameters. In Fig. 6.23(b), we only used the region of tagged photon energy where the TS resolution is smaller than 60 % of the CsI resolution. The same energy region determined this way was applied to all subsequent plots on energy resolution. The fitting method also has an influence on the result. They are, for example, the fitting region, the initial parameter setting, the value of fixed asymmetry parameter and the shape of background contribution. The effect from these factors were checked by varying the parameter and by applying different procedures for the fitting. The effect was mostly negligible except for one described below.

For the fitting of R_E, the cut off is set at 20 % of the peak value to remove the tail part from the fitting. The χ^2 of the fitting usually became best at that value.

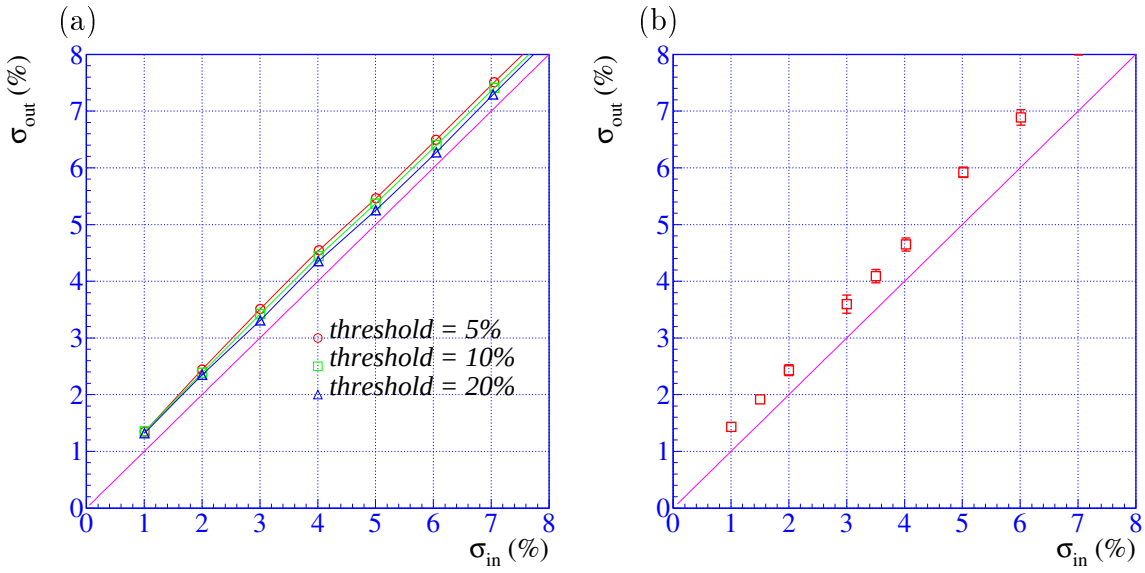

Figure 6.33: (a)Correlation of the generated R_E resolution σ_{in} and obtained resolution σ_{out} after fitting and subtraction of the TS resolution with $\sigma_{TS} = 3.3\%$. (b)Results of the same practice for the Compton edge resolution.

The variation of the fitting for different cut off value are shown in Fig. 6.32 for the R_E distribution at $E_\gamma = 25$ MeV. When the cut off value was changed, the result of resolution changed between 4.5 % and 5.3 %.

For the purpose of checking the fitting procedure, we made a simple Monte Carlo program. We produced the distribution of R_E $(= \frac{E_{CsI}}{E_{TS}})$ by generating E_{CsI} by the logarithmic Gaussian and E_{TS} by the Gaussian. Then we fitted R_E by the logarithmic Gaussian and subtracted the resolution of E_{TS} quadratically from the resolution of R_E to obtained the resolution of E_{CsI} (see section 6.7.1). This is the same procedure as we used to get σ_E from the data. Fig. 6.33 shows the result with $\eta = 0.47$ and $\sigma_{TS} = 3.3$ % corresponding roughly to the photon energy of 30 MeV. The different marks mean the different cut-off thresholds used to determine the fitting region. If our fitting procedure is perfect, the E_{CsI} resolution obtained after fitting $(=\sigma_{out})$ should be equal to the E_{CsI} resolution used for the generation $(=\sigma_{in})$. The results have some systematic deviation from $\sigma_{out} = \sigma_{in}$ line. This is because the energy spectrum of CsI is not Gaussian and the tagging system resolution is not perfectly subtracted.

The same study is done to the Compton edge fitting. Theoretical Compton distribution (6.1) is generated and convoluted with the CsI response function. The fitting result given in Fig. 6.33 shows a similar systematic shift.

For every photon beam setting, we repeated the measurement four times, and for

each time the beam was injected at the center of one of the four central crystals. The error bars in Fig. 6.23 is not statistical error but the rms deviation of four measurements. We note that the results obtained by three methods (R_E, Compton and Bremsstrahlung edge) are in good agreement each other. The results of R_E from different electron beam settings overlaps in the same energy region. Considering different methods have different systematics, we think the error bars assigned to the Fig. 6.23 from the rms deviation of four measurements are realistic. An estimate of additional systematic error is difficult, but the simulation study of fitting procedure described above suggests it is at the level of 0.5 %.

6.8 Energy Linearity

6.8.1 Compton Edge and Bremsstrahlung Edge

The energy linearity is analyzed by using the edge values of the Compton and Bremsstrahlung distribution. The information of the tagging system was not used for this analysis to avoid additional complication from the non-linearity of the TS response.

The Compton edge and Bremsstrahlung edges are fitted with the convolution of the theoretical distribution and the CsI response function as explained in the previous section. The values obtained from the fitting of the data E_{CsI} and the theoretical edge value E_{TH} calculated from the electron beam energy are plotted in Fig. 6.34(a). The value of E_{CsI} is calculated as the 5×5 matrix sum with 0.5 MeV threshold. The deviation from the linear response, $(E_{CsI} - E_{TH})/E_{TH}$, is plotted in Fig. 6.34(b). The error is estimated in section 6.8.3. For all the energy ranges, the deviations are negative because of the shower leakage from the central 5×5 counters. The leakage from the back of the crystal becomes dominant at high energy and makes a larger negative deviation.

6.8.2 Comparison with Monte Carlo Simulation

The same GEANT setup is used for the resolution analysis. The deviation from the linear behavior is shown in Fig. 6.35. The error bar is the rms of four different runs. The shower leakage effect found in the higher energy data is well reproduced by the Monte Carlo. The deficiency of energy deposit in the lower energy is caused by the non-uniformity of CsI crystals. The results with perfectly uniform crystal is shown in Fig. 6.36 to demonstrate this effect.

(a)

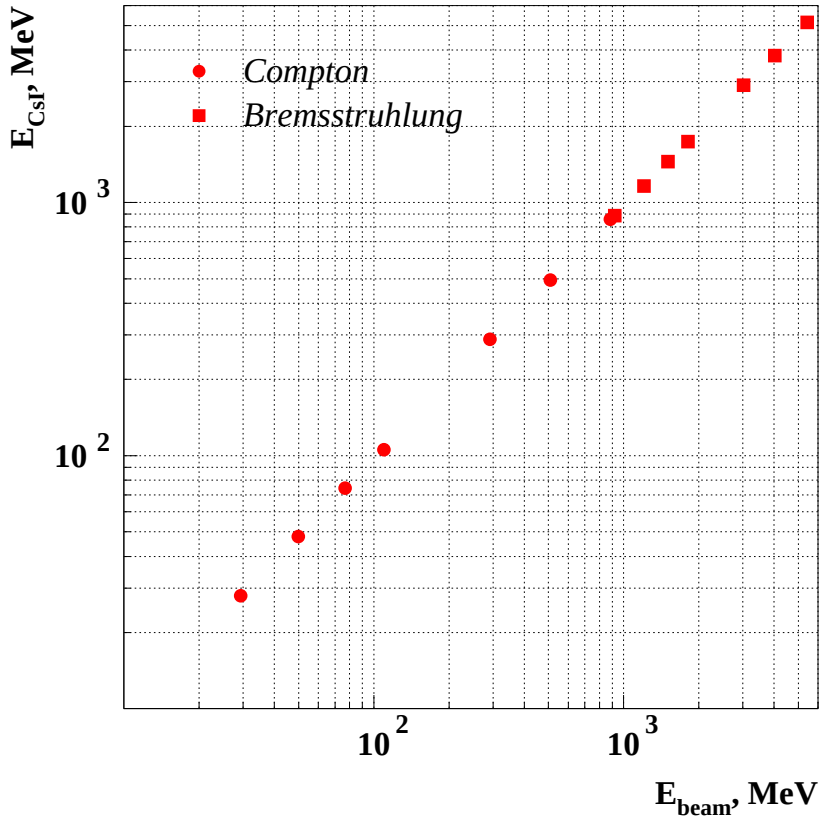

(b)

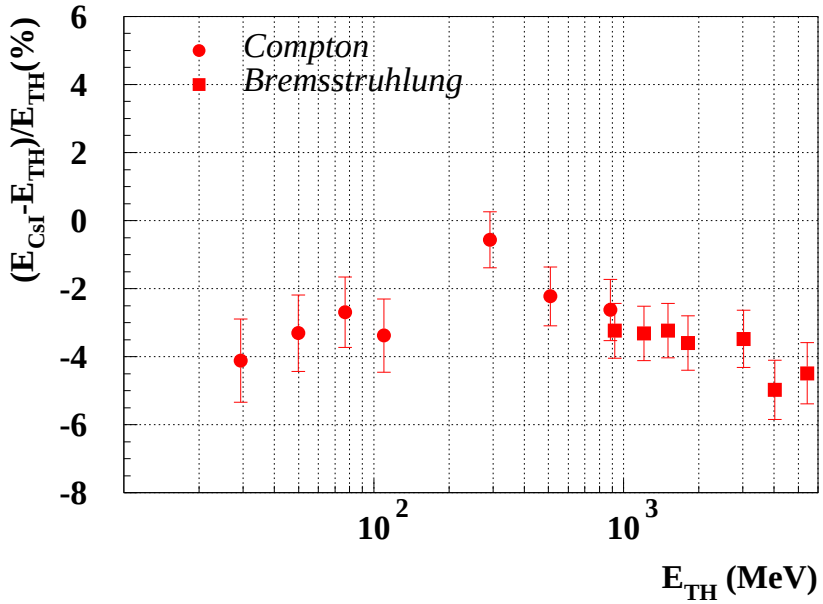

Figure 6.34: (a)Incident photon beam energy vs measured energy in CsI for data. (b)Energy linearity for data.

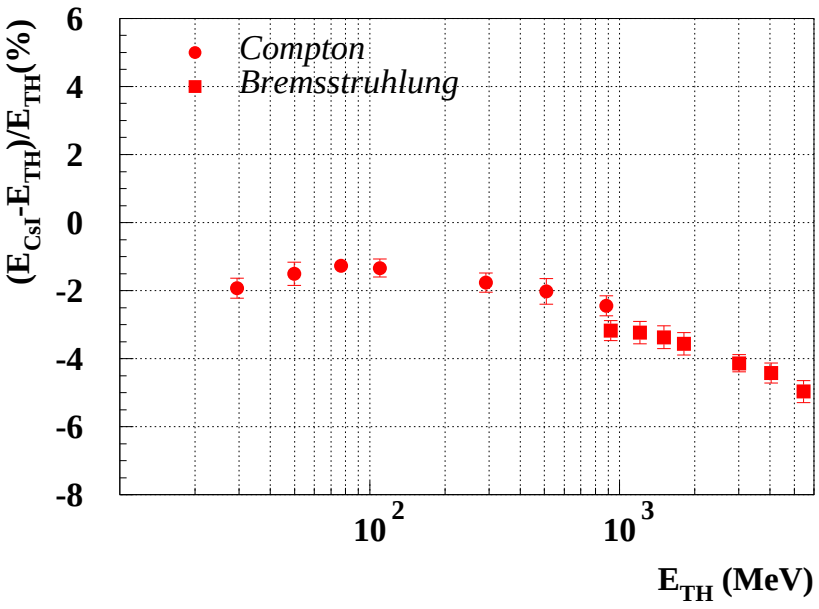

Figure 6.35: Energy linearity for MC.

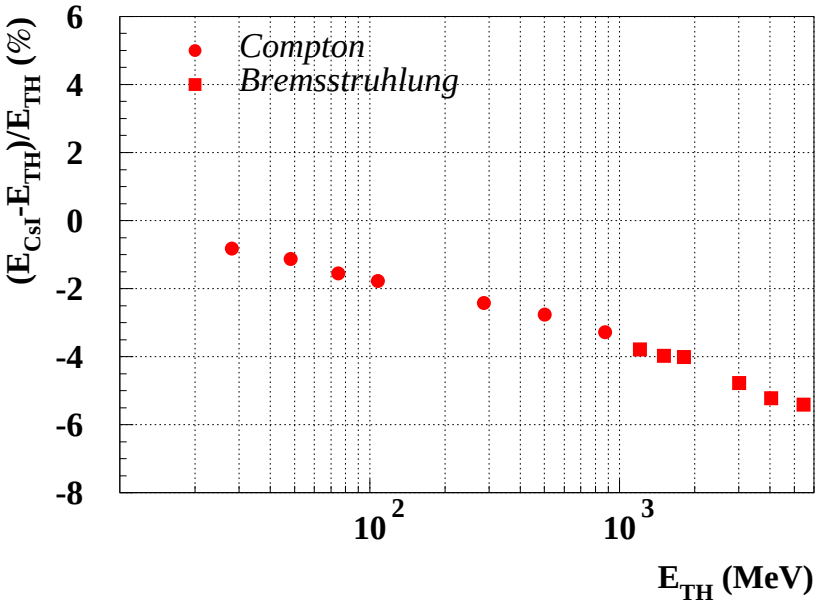

Figure 6.36: Energy linearity for Monte Carlo simulation. Perfectly uniform light output is assumed.

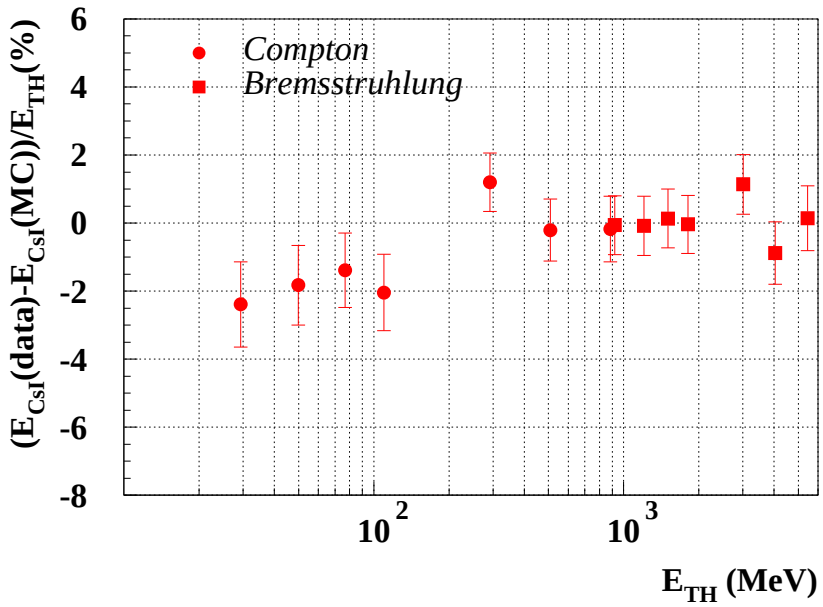

Figure 6.37: Difference of energy linearity between data and M.C.

Fig. 6.37 show the difference between real data (Fig. 6.34) and simulation results (Fig. 6.35). The differences are within ± 2 % for all energy range.

6.8.3 Discussion

An estimate of errors for the linearity plot is tabulated in Table. 6.2. We explain each source of errors in the following.

The statistical error is obtained by the MINUIT routine of the fitting. It is larger at low energy but is still at the negligible level.

All counters are calibrated at the photon beam energy of 508 MeV. Different light collection uniformity can make a different linearity behavior for the four counters tested. The rms deviation of four counters becomes larger in the low energy region and it seems to support this idea. Some of the data points were measured more than once and the rms in the Table. 6.2 also includes the effect of time dependent factor.

As discussed in section 6.6, the time dependence of the calibration constant is followed by the cosmic-ray calibration. Fig. 6.38 shows the correction factor applied for the Compton photon run. The deviation is less than 1% and we guess it is mainly the temperature effect. We assign 0.5 % error to the temperature dependence of the calibration constant.

The incident beam position also affects the energy deposit in the crystal. The beam was targeted at the center of the crystal for all runs in all the energy ranges. But it

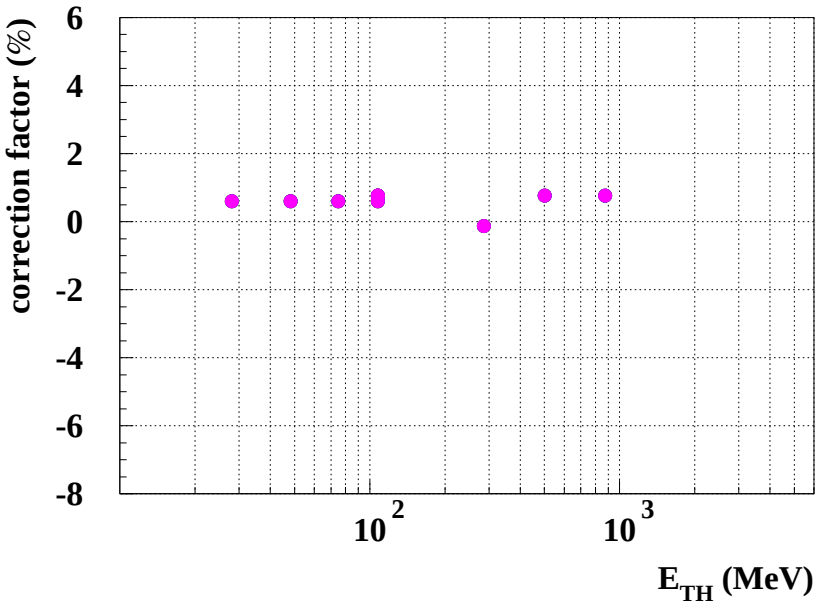

Figure 6.38: Time dependent correction factor determined by cosmic calibration. The reference point is the cosmic data nearest to the beam calibration run, which is not included in this plot.

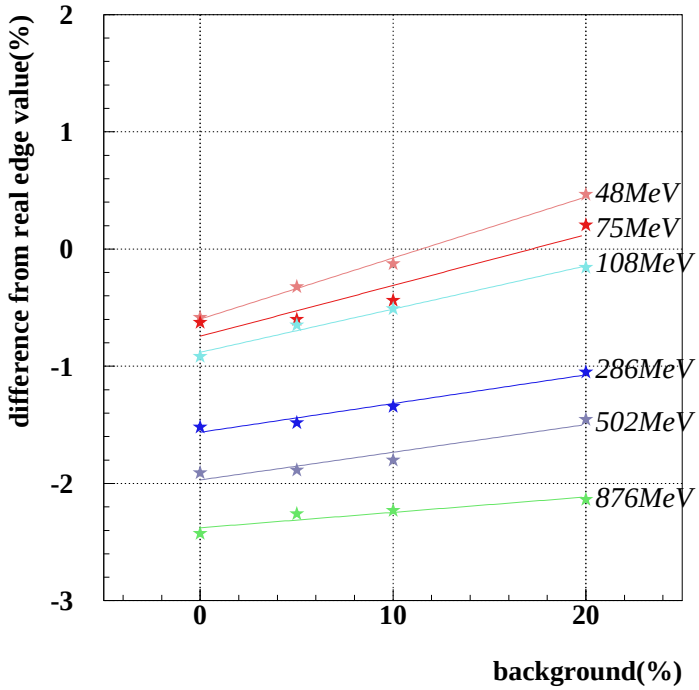

Figure 6.39: Variation of fitted Compton edge with different amount of 2 photon background simulation study.

(a)

Error source vs. Beam Energy	29.4	49.8	76.8	109.8	291.5	508.3	884.7
statistical error from MINUIT	0.13	0.06	0.03	0.02	0.006	0.003	0.002
variation among 4 counters	0.84	0.80	0.77	0.74	0.19	0.15	0.13
temperature	0.5	0.5	0.5	0.5	0.5	0.5	0.5
incident point	-	0.03	0.015	0.015	-	-	-
background	0.4	0.4	0.28	0.31	0.18	0.08	0.09
fitting procedure	0.25	0.15	0.10	0.11	0.07	0.05	0.12
electronics linearity	0.3	0.3	0.3	0.3	0.3	0.3	0.3
pedestal measurement	0.30	0.21	0.21	0.18	0.11	0.079	0.057
Electron beam energy estimation	0.33	0.21	0.13	0.36	0.50	0.60	0.66
quadratic sum	1.22	1.12	1.04	1.08	0.82	0.86	0.90

(b)

Error source vs. Beam Energy	921.	1206.	1506.	1810.	3007.	4036.	5441
statistical error from MINUIT	0.08	0.08	0.05	0.05	0.11	0.09	0.11
variation among 4 counters	0.53	0.53	0.53	0.53	0.53	0.53	0.53
temperature	0.5	0.5	0.5	0.5	0.5	0.5	0.5
incident point	-	-	-	-	0.008	-	-
background	-	-	-	-	-	-	-
fitting procedure	0.05	0.10	0.10	-	0.05	0.15	0.20
electronics linearity	0.3	0.3	0.3	0.3	0.3	0.3	0.3
pedestal measurement	0.01	0.008	0.007	0.005	0.003	0.002	0.001
Electron beam energy estimation	0.16	0.10	0.07	0.04	0.26	0.32	0.36
quadratic sum	0.81	0.80	0.80	0.80	0.84	0.87	0.90

Table 6.2: Systematic error estimation of (a)Compton photon and (b)Bremsstrahlung photon(unit : %).

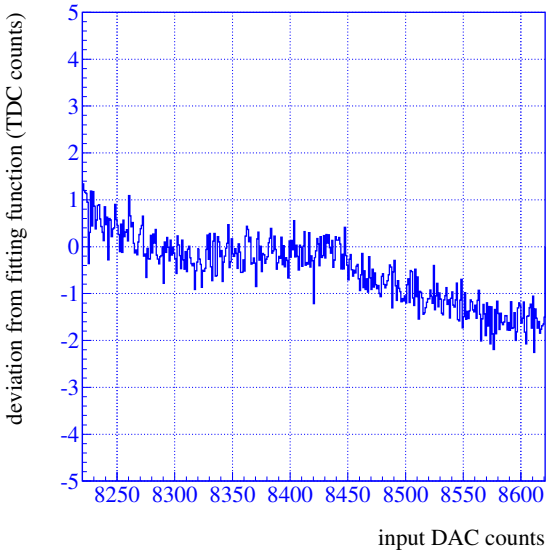

Figure 6.40: Electronics linearity measured by the test pulse for $0 - 100$ MeV.

sometimes shifted a few mm in the center of gravity position (X_c,Y_c). The displacement of δX_c or $\delta Y_c \equiv 0.1$ causes the 0.03 % energy shift. From the beam position of each run, we calculated the amount of energy shift and listed them in the Table. 6.2.

The Compton distribution has the 2 photon background and it is modeled as a triangular shape in the fitting routine (see Fig. 6.20). If the background estimation is not correct, the Compton edge value has some shift. By using a simple Monte Carlo program, we generated smeared Compton spectrum with different amount of 2 photon backgrounds. They are fitted by the flat and triangular shape of background and the values of obtained Compton edge are compared. The results are shown in Fig. 6.39. The difference also depends on energy. The real background of the data was different run by run but it was less than 10 %. The estimated error is listed in the Table. 6.2.

The Compton edge value obtained by the fitting varies with the fitting region. For the values shown in Fig. 6.34, the fitting region is limited to $\pm$ 5 σ around the Compton edge obtained by the first preliminary fitting. In order to estimate the effect, the fitting region was changed to 50 $\sim$ 180 % and 90$\sim$ 120 % of the edge value. The difference is 0.1 $\sim$ 0.5 MeV in all the energy ranges and its effects listed in the Table. 6.2.

The electronics linearity is good as mentioned in section 6.5.2. However, a special electronics calibration was done to check the linearity especially in low energy range. Fig. 6.40 shows the result corresponding to the energy region of 0 $\sim$ 100 MeV. In the energy region lower than 50 MeV, the deviation was $\pm$ 1 TDC count and it corresponds

to 100 keV.

We also made a special source test of the electronics to confirm the linearity below 2.5 MeV. We prepared a small CsI(Tℓ) crystal and attached the photomultiplier and the photodiode at both ends of the crystal as shown in Fig. 6.41(a). A ^{137}Cs was placed on the crystal and a ^{60}Co was buried in the crystal. The spectra obtained are shown in Fig. 6.41(b) and (c) for photomultiplier and photodiodes. The photopeaks at 0.662 MeV for ^{137}Cs, 1.173 and 1.333 MeV for ^{60}Co are clearly seen for the phototube in Fig. 6.41(b). The peak produced by the sum of 2 γ's (2.506 MeV) is also seen. We selected the event in the photopeak region by the photomultiplier data and plotted the distribution of the photodiode data. The photodiode data correspond to 0.662 MeV photopeak is shown in Fig. 6.41(e). The peak of this distribution corresponds to the energy deposit of 0.662 MeV in the crystal detected by the photodiode.

We collected two more sets of data by reducing the amount of light collected by the photodiode by a factor of $\sim$2 and $\sim$4. All three sets of data are fitted by a line keeping the ratio of four peak positions within one set constant (0.662 : 1.173 : 1.333 : 2.506) and only changing the scale between three sets. The result is shown in Fig. 6.42. The linearity is $\pm$ 0.5 % from 0 to $\sim$2.5 MeV*. This proves the good linearity of the electronics in the low energy region, independently from the test pulse measurement.

For the linearity analysis, we obtained the pedestal value for each run from the empty trigger mixed in the usual data taking trigger. In this way, we avoided the effect of drift from the pedestal values taken by the pedestal run. This was necessary because the Compton edge at low energy is sensitive to a small shift of the pedestal value. We estimate the error of the pedestal is 0.5 TDC counts and it corresponds to $\sim$ 35 keV.

The theoretical energy of the Compton or Bremsstrahlung edge E_{TH} also has a systematic error coming from the uncertainty of the electron beam energy. The nominal electron beam energy of VEPP4 storage ring was calibrated by using the harmonics of Nd:YAG laser. The laser can produce two harmonics ; the first harmonic corresponds to w = 1.1654 eV and the second harmonics is at w = 2.3308 eV. We can produce the some Compton spectrum by the 2nd harmonic with electron beam energy E_1 and by the 1st harmonic with electron beam energy E_2 ($E_1 < E_2$). As the ratio E_1/E_2 for the same Compton edge energy can be exactly calculable, we can measure the electron beam energy E_2 if we know the energy of E_1 exactly. Experimentally, the energy of E_1 was calibrated by the J/ψ observation by the KEDR experiment where VEPP4 was operated in e^+e^- collision made. We used our CsI matrix to check the Compton edge

*The energy scale of Fig. 6.42 is consistent within 10 % with the large crystal to be used in the BELLE experiment.

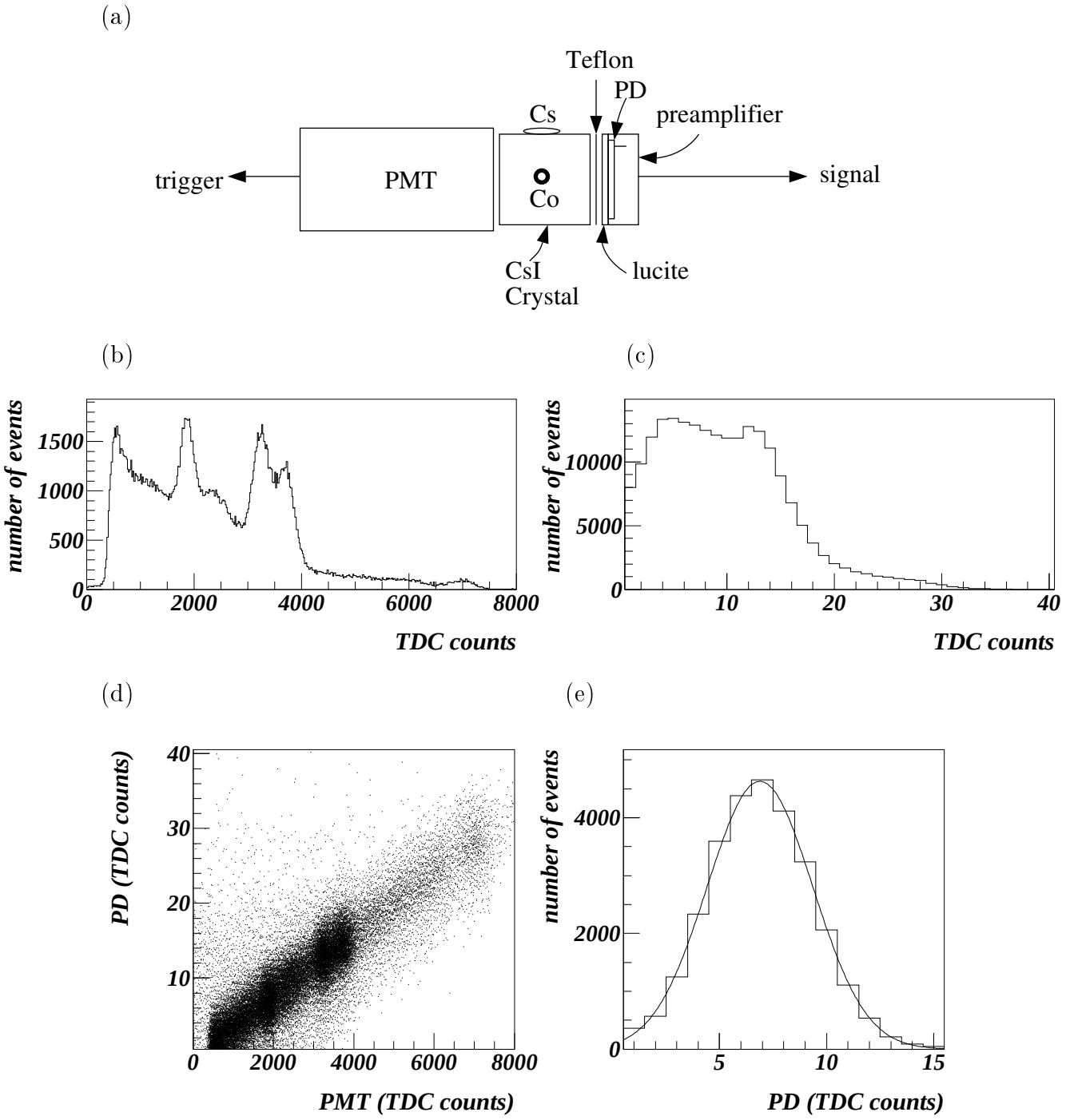

Figure 6.41: (a)Setup of the linearity measurement by using the ^{137}Cs and ^{60}Co sources and the spectrum with (b)photomultiplier and (c)photodiodes. (d)Correlation between photomultiplier data and photodiode data. (e)Photodiode spectrum corresponding to 662 keV ^{137}Cs photopeak selected by the photomultiplier data.

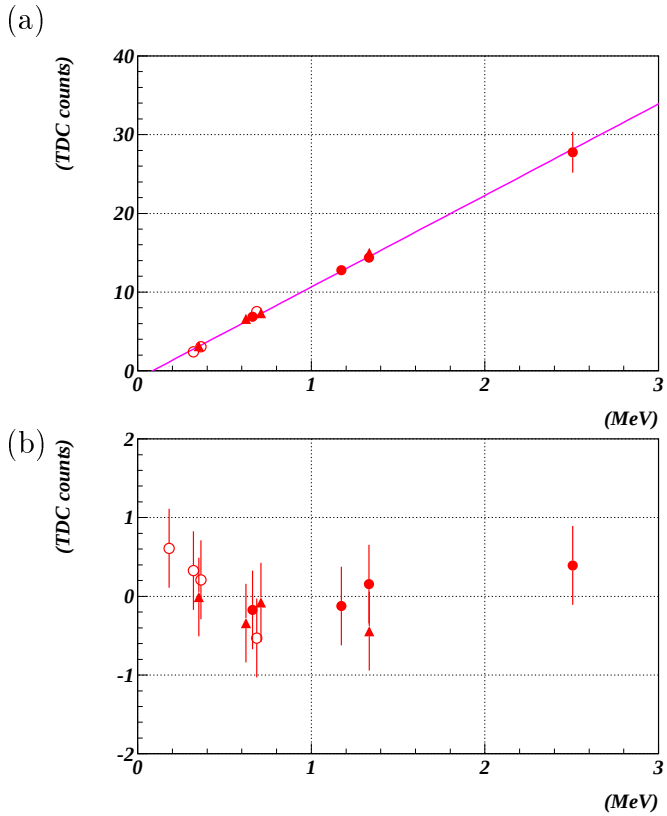

Figure 6.42: (a)Energy linearity measured by using the ^{137}Cs and ^{60}Co and (b)deviation from the linear response.

of E_1 is the same as the Compton edge E_2. As two edge energies could not be adjusted exactly, we applied a small correction on E_2 calculated from the energy difference of two edge energies. The electron beam energy was calibrated between $1090 \sim 4269$ MeV in 5 steps by this method and corrections of $20 \sim 30$ MeV were made. From the error of this correction, the E_{TH} error is calculated. It is larger at high energy because the beam energy was successively calibrated from J/ψ energy upward [70].

6.9 Summary and Conclusion

The performance of the BELLE calorimeter prototype based on 6×6 matrix counters was studied with tagged Compton photon and Bremsstrahlung photon beam in the energy range from 20 MeV to 5.4 GeV. The energy resolution is 5.8 % at 20 MeV and 1.8 % at 5.4 GeV when the energy deposit in 5×5 counters are summed up. We found the resolution improves significantly when 0.5 MeV threshold is applied. The result with threshold is 5×5 counters is 4 % at 20 MeV. The measured Compton spectrum and the resolution of CsI are in excellent agreement with the GEANT Monte Carlo.

The energy deposit in 5×5 matrix with 0.5 MeV threshold is -3 ± 2 % of the injected photon energy for 20 MeV $\sim$ 5.4 GeV. The energy dependence of the energy deposit (linearity) is well reproduced by GEANT above 300 MeV. Below 100 MeV the data shows $\sim$ 2 % lower energy deposit than GEANT expects. The observed non-linearity can be corrected by the response function and by the use of GEANT simulation in BELLE experiment.

The electronics noises are 16.5 keV and 189 keV for the coherent and incoherent noise. The performance of the electronics designed for BELLE was thoroughly tested by the photon beam and was proven to be excellent.